ACS Biomaterials SCIENCE & ENGINEERING

Article

Nanoligomers Targeting Human miRNA for the Treatment of Severe COVID-19 Are Safe and Nontoxic in Mice

Colleen R. McCollum, Colleen M. Courtney, Nolan J. O'Connor, Thomas R. Aunins, Yuchen Ding, Tristan X. Jordan, Keegan L. Rogers, Stephen Brindley, Jared M. Brown, Prashant Nagpal, and Anushree Chatterjee*

Cite This: https://doi.org/10.1021/acsbiomaterials.2c00510

Read Online

ACCESS | Metrics & More | Article Recommendations | Supporting Information

ABSTRACT: The devastating effects of the coronavirus disease 2019 (COVID-19) pandemic have made clear a global necessity for antiviral strategies. Most fatalities associated with infection from severe acute respiratory syndrome coronavirus 2 (SARS-CoV-2) result at least partially from uncontrolled host immune response. Here, we use an antisense compound targeting a previously identified microRNA (miRNA) linked to severe cases of COVID-19. The compound binds specifically to the miRNA in question, miR-2392, which is produced by human cells in several disease states. The safety and biodistribution of this compound were tested in a mouse model via intranasal, intraperitoneal, and intravenous administration. The compound did not cause any toxic responses in mice based on measured parameters, including body weight, serum biomarkers for inflammation, and organ histopathology. No immunogenicity from the compound was observed with any administration route. Intranasal administration resulted in excellent and rapid biodistribution to the lungs, the main site of infection for SARS-CoV-2. Pharmacokinetic and biodistribution studies reveal delivery to different organs, including lungs, liver, kidneys, and spleen. The compound was largely cleared through the kidneys and excreted via the urine, with no accumulation observed in first-pass organs. The compound is concluded to be a safe potential antiviral treatment for COVID-19.

KEYWORDS: antisense therapy, COVID-19, host immune response, safety, biodistribution
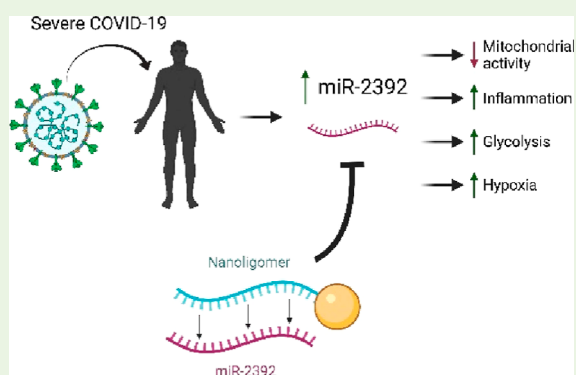
INTRODUCTION

With the global spread of severe acute respiratory syndrome coronavirus 2 (SARS-CoV-2) beginning in early 2020, the lack of options for antiviral treatments to respiratory infections became starkly apparent. SARS-CoV-2, an enveloped positive-stranded RNA virus, infects the respiratory system of humans by recognizing the human receptor angiotensin-converting enzyme 2 (ACE2)[1] in synergy with the transmembrane protease receptor, serine 2 (TMPRSS2),[2] in epithelial cells of, first, the respiratory tract and then the lungs, causing coronavirus disease 2019 (COVID-19). As the virus replicates, a combination of the host immune response and viral damage to cells can result in severe cytokine storm syndrome, acute respiratory distress syndrome, and respiratory failure.[1,3,4] COVID-19 may also cause cardiovascular, liver, gastro-intestinal, kidney, and neurological injury.[5] At the time of writing, COVID-19 has caused over 437 million cases of illness and nearly 6 million deaths globally.[6] While multiple vaccines have been developed,[7−9] the occurrence of new variant strains and the low rates of vaccination or lack of vaccine availability in some regions of the world threaten the efficacy of these vaccines in keeping the global population safe.[5] Current

treatments for patients with severe COVID-19 mainly focus on controlling the immune response[10] or providing organ support,[11] but while most patients recover from the disease, lasting effects may continue to disrupt patient lives[12] and global fatalities remain high.

Antisense oligonucleotides (ASOs) are short single-stranded sequences of synthetic nucleotides capable of binding organic nucleic acids and include molecules such as peptide nucleic acids (PNAs), synthetic small interfering RNAs (siRNAs), and morpholinos.[13,14] PNAs are macromolecules comprising nucleobases on a pseudo-peptide backbone.[15,16] They are rigid with a long half-life in vivo.[17] The PNA backbone is uncharged, which eliminates electrostatic repulsion that DNA and RNA strands experience with DNA−RNA and DNA−
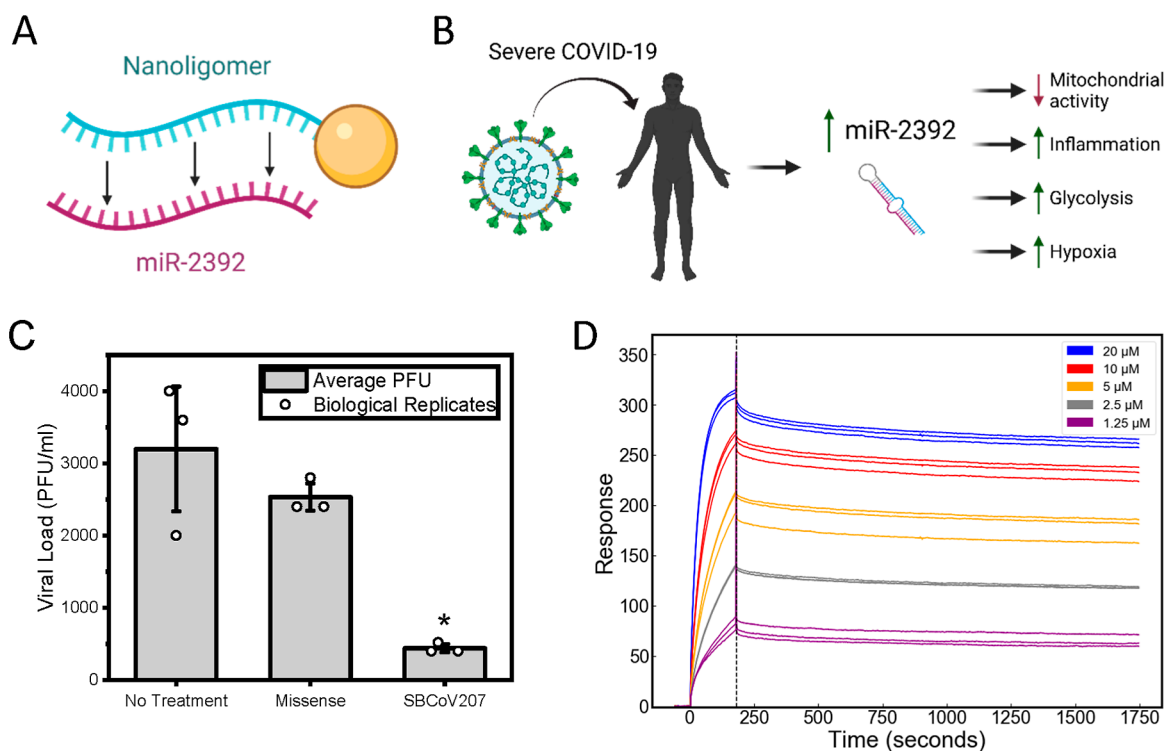
Figure 1. Nanoligomers target miRNA using PNA-based sequence-specific attachment (A). Here, Nanoligomers (SBCoV207) are targeted to miR-2392, which is upregulated in severe cases of COVID-19 (B). A single dose of 10 μM of SBCoV207 is able to reduce plaque-forming units (PFUs) of virus (C) in infected Vero E6 cells, while missense PNA targeting no sequence in the viral or human circulating RNA do not result in a significant drop in viral load at this concentration ($n = 3$). SBCoV207 binds to the target miRNA sequence miR-2392 with a K_D of 48.11 nM and an association rate constant (k_a) of 1372 M^{-1} s^{-1} according to surface plasmon resonance (SPR) measurements (D).

DNA binding, thus allowing for stronger binding to DNA and RNA.[15] PNA can thus be utilized as inhibitory therapeutics that tightly attach to their target, in comparison to DNA-based technologies optimized for the dynamic kinetics of DNA binding.[18−20] PNAs can be synthesized in specific base pair sequences complementary to desired targets in an RNA or DNA genome. Furthermore, PNAs have previously been applied to specifically bind miRNAs and modulate immune response,[21] fight tumors,[22] detect biomarkers,[23] or serve as biosupramolecular tags.[24] However, until recently, antisense technologies have faced a variety of challenges in clinical translation despite their versatility in targeting nucleic acid sequences. Nucleic acids typically require a delivery vehicle to pass into cells. While PNAs conjugated to cell penetrating peptides (CPPs) can elicit immune response,[25] other delivery forms such as liposomes and cationic lipid encapsulation have also caused reactions from the innate immune system.[26,27] The use of polyethylene glycol resulted in issues with immune response and inhibited cellular uptake.[26,27] siRNA can independently elevate the innate immune response as well,[28,29] with success in avoiding this seen in only some platforms.[30,31]

Here, we test the safety of peptide-based Nanoligomer molecules developed by Sachi Bioworks. The sequence specific PNA component is specifically targeted to treat COVID-19, whereas a conjugated nanoparticle facilitates delivery (Figure 1A). Various factors in both the infecting virus and the host body result in severe symptoms of respiratory infection. MicroRNAs (miRNAs), small and non-coding RNAs, serve a number of functions in the human body, including post-transcriptional regulation of genes associated with infection

response.[32] Following infection, the landscape of miRNA present in the circulation can change, indicating the importance of miRNAs in modulating the host immune response.[33−35] In humans, elevated levels of miRNA 2392 (miR-2392) have been linked to severe response to COVID-19.[36] Furthermore, studies indicate that certain miRNA may be regulated by the viral genome to promote viral replication and spread or limit host immune response.[32,35,37−40] It has been demonstrated that miR-2392 may be one such target (Figure 1B).[41] Mitochondrial suppression[42] and upregulation of inflammation, glycolysis, and hypoxia have been linked with higher miR-2392 levels, and increased miR-2392 correlated with severity of SARS-CoV-2 viral load.[41] Our Nanoligomer SBCoV207 was designed to target miR-2392.

Nanoligomers contain gold nanoparticles to improve transport because gold is a highly nonreactive and biocompatible metal.[43−45] Naked PNAs typically exhibit poor uptake into mammalian cells due to their large size and lack of charge.[15] While CPPs may be added to PNA to facilitate transport, these peptides may cause an immune response in the cells.[46] Gold nanoparticles of less than 15 nm diameter have shown widespread biodistribution throughout the body.[47,48] Prior to this report, we note that stable conjugation of PNA to gold nanoparticles has been successful only in a few cases.[49−52]

Previously, we have shown that A549-ACE2 human lung epithelial cells uninfected with SARS-CoV-2 showed no signs of toxicity at 40 μM Nanoligomer doses, and treatment with the SBCoV207 Nanoligomer targeted to miR-2392 improved cell viability in A549-ACE2 cells infected with SARS-CoV-2 and resulted in 85% viral inhibition at a dose of 10 μM.[41] In a separate study, Syrian hamsters infected with SARS-CoV-2 and
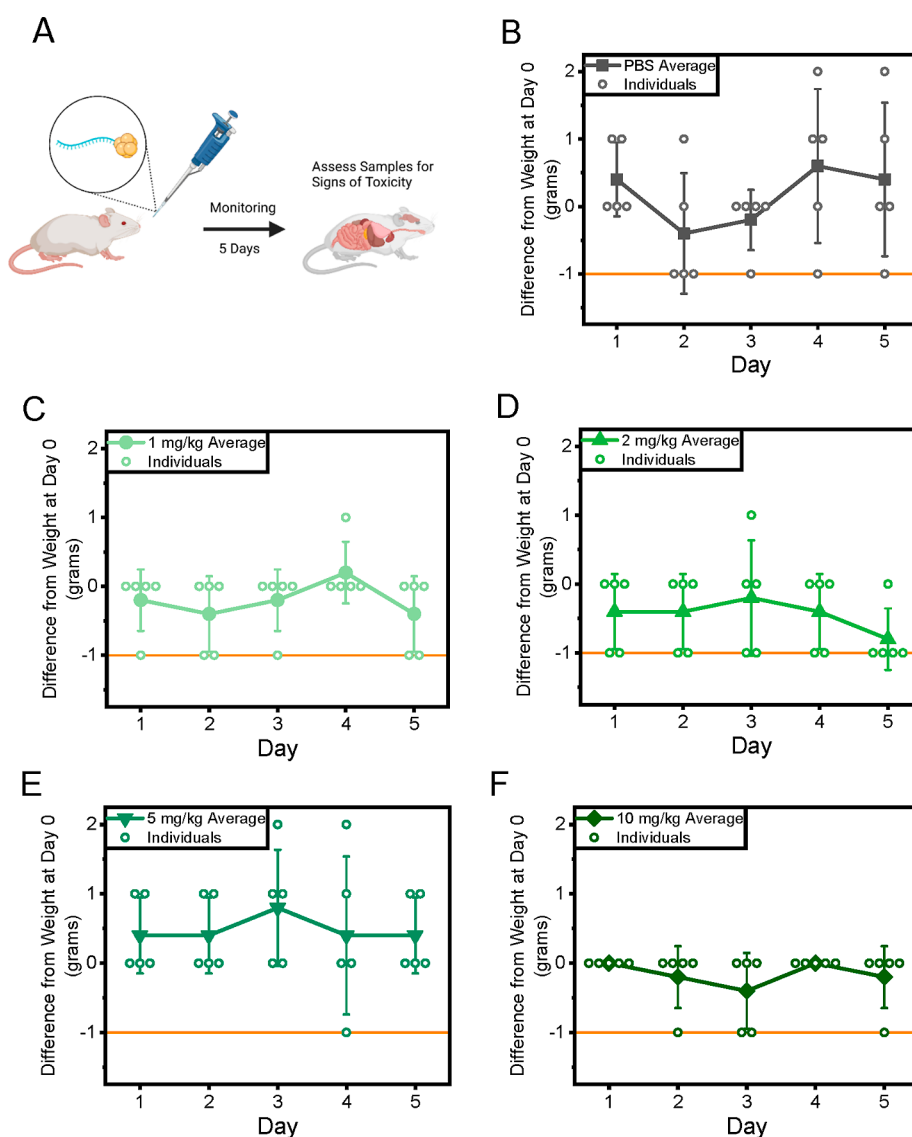
Figure 2. Intranasal administration of SBCoV207 did not cause weight loss in mice. Mice were administered with SBCoV207 intranasally and monitored for 5 days (A). Body weight did not drop more than 1 g below starting weight for any mouse (B–F). The horizontal orange line is used to indicate 1 g below the weight on day 0 of the study. The p value was greater than 0.05 for all groups and time points compared to the PBS control group (B). $n = 5$ for each dose, as indicated by circular points.

treated with only 0.13 mg/kg of Nanoligomers showed lower viral titers than hamsters receiving a control treatment of saline.[41] Furthermore, Syrian hamsters administered with Nanoligomers showed no changes in the behavior.[41] However, as Nanoligomers are a new modality of disease treatment, we require a greater understanding of their safety, biodistribution, and pharmacokinetics (PK) in vivo.

Here, we test SBCoV207 treatment in a murine model of safety and biodistribution. Intranasal administration was chosen as the preferred route of drug administration due to the direct application of treatment to the infection site.[53–55] This allows for the treatment compound to be at its highest concentration where the infection is most prevalent and then safely biodistributed and excreted from the body.[55] Intranasal administration is simple and efficient in a murine model[56] and eliminates the concerns of compound reaching the respiratory systems at insufficient concentrations for efficacy, as could be the case with intravenous and intraperitoneal injection.[57] Intraperitoneal and intravenous administration routes were

also explored to provide a thorough assessment of the biodistribution of Nanoligomers. Intraperitoneal injections are often considered a simpler method for assessing first-pass metabolism and clearance of a compound, compared to orally administered methods, and does provide valuable information on target engagement with and transport through various bodily systems.[57] Intravenous injections, in this case via the tail vein of mice, allows for the assessment of compound accumulation in any organs that receive significant blood flow, including the kidneys, lungs, and liver.

The Nanoligomer treatment SBCoV207 shows promise as a treatment for SARS-CoV-2 infection, filling a void where there are limited antiviral treatments currently on the market. Here, we test the safety of this treatment in a murine model and assess the biodistribution and clearance pathways involved.

■ RESULTS

SBCoV207 Targets miR-2392. Vero E6 cells infected with SARS-CoV-2, treated with 10 μM of SBCoV207 and assessed
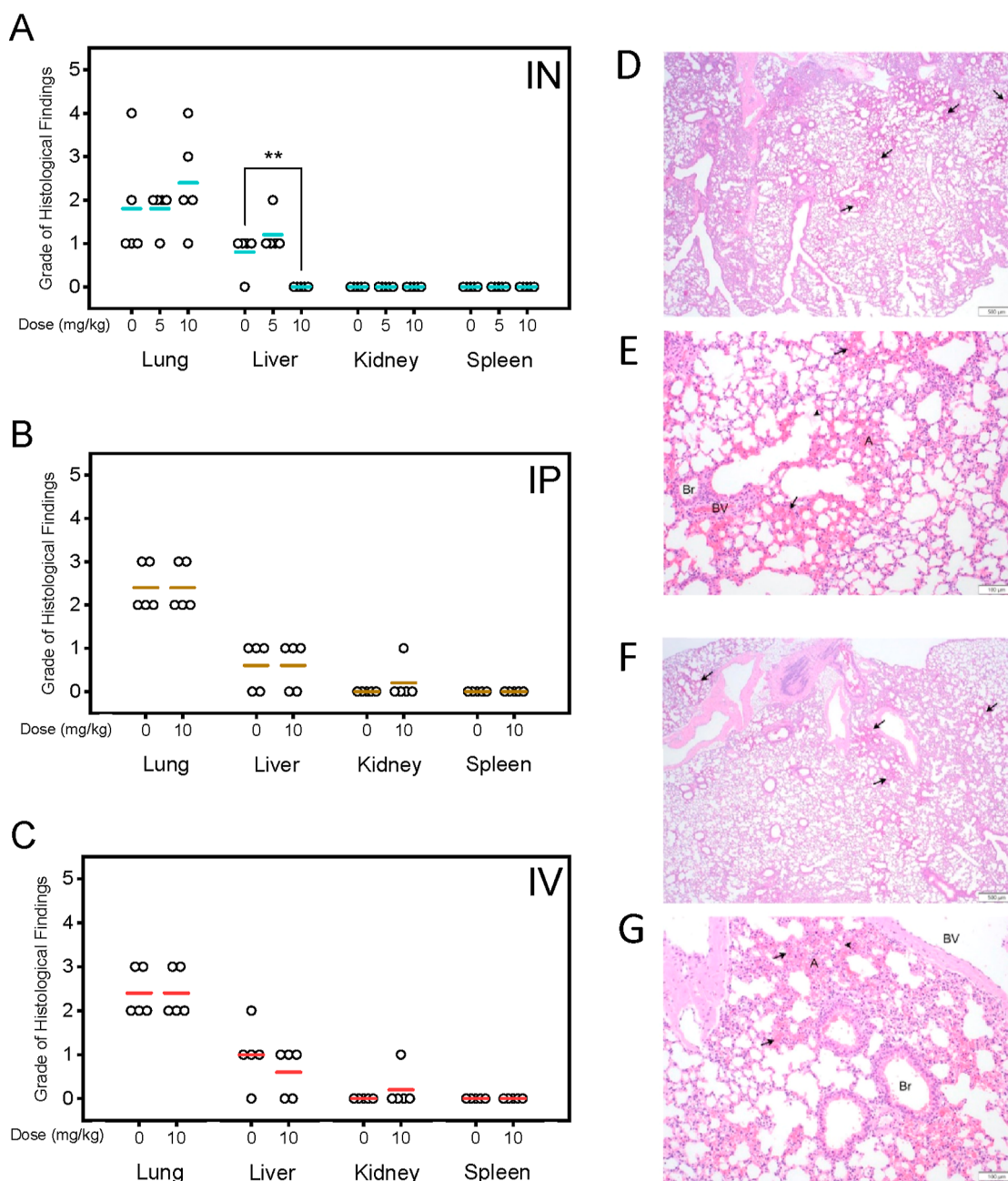
Figure 3. Administration of SBCoV207 did not result in significant changes to morphology of lung, liver, kidney, or spleen based on histology with hematoxylin and eosin (H&E) staining (A−C), regardless of the administration method. Histology was graded on a 0−5 scale with 0 = absent, 1 = minimal, 2 = mild, 3 = moderate, 4 = marked, and 5 = severe. The administration method is indicated in the right (A−C) corner of each plot and colored bars represent mean. ** indicates $p < 0.01$, otherwise $p > 0.05$. $n = 5$ for each dose. Lungs of mice treated intranasally with the PBS control (D,E) showed hemorrhaging of comparable severity to mice treated with 5 mg/kg IN SBCoV207 (F,G). Multifocal regions of hemorrhage (arrows) are observed throughout the parenchyma, often adjacent to blood vessels, and characterized by free red blood cells within alveoli (A) and bronchioles (Br). Hemorrhage is sometimes accompanied by eosinophilic proteinaceous material (fibrin; arrowhead). Images taken at 20× (D,F) and 100× (E,G) magnification.

for viral load using a plaque assay 24 h post infection and treatment, showed significant reduction in viral PFUs ($p = 0.011$, Figure 1C). As a negative control, a missense Nanoligomer targeting no predicted circulating miRNA, mRNA, or viral genome sequences was used. This missense Nanoligomer reduced the number of PFU per ml when compared with the no-treatment group.

To further confirm the efficacy of SBCoV207 against SARS-CoV-2 infection, human lung epithelial cells expressing human ACE2 (A549-hACE2) infected with SARS-CoV-2 were treated

with SBCoV207 and then fixed and immunostained for the viral nucleocapsid (N) protein. SBCoV207 consistently inhibited viral infection compared to missense Nanoligomers at concentrations ranging from 0.078 to 10 μM (Figure S1A). At 10 μM concentration, Nanoligomers significantly reduced the percent of infected cells when compared to no treatment ($p = 0.00025$, Figure S1B).

The abundance of viral mRNA transcriptional regulatory sequence N-protein (TRS-N) was measured by quantitative reverse-transcription polymerase chain reaction (qRT-PCR) in

infected A549-hACE2 cells treated with 10 μM SBCoV207 or missense Nanoligomers and normalized to abundance in cells treated with an equal volume of a water control (Figure S1C). The TRS-N abundance is correlated with overall viral abundance, as it is found in the genome of each viral particle.[58] SBCoV207 treatment resulted in a nearly 10-fold reduction in viral mRNA abundance. Interestingly, the missense Nanoligomer control reduced viral mRNA abundance as well to a lesser extent not statistically different from the SBCoV207 group, indicating the possibility of a mild baseline effect of Nanoligomers against SARS-CoV-2 regardless of the sequence, though the mechanism of such an effect would be unknown.

To quantify the binding affinity of SBCoV207 to its complimentary target, we performed SPR measurements on different concentrations of Nanoligomers flowed over a DNA oligomer containing fragments of the human genome with the miR-2392 target sequence (Table S1). SBCoV207 binds to this target in an anti-parallel orientation, which is the preferred orientation for strong PNA−DNA or PNA−RNA interactions.[59] The binding response was measured during analyte injection (Figure 1D, up to vertical dashed line) and the resulting fit yielded an association rate constant (k_a) of 1372 $M^{-1} s^{-1}$. Subsequent dissociation was slow (dissociation rate constant $k_d = 6.56 \times 10^{-5} s^{-1}$), which is characteristic of PNA bound to nucleic acid targets.[60] Using these results, we found that SBCoV207 strongly binds its complementary target with a measured dissociation constant K_D of 48.11 nM. We also performed SPR measurements on the missense Nanoligomer binding with the same DNA oligomer containing the miR2392 binding sequence. The response at different missense Nanoligomer concentrations was low (Figure S1D), suggesting negligible levels of nonspecific binding. These data provide in vitro evidence that SBCoV207 can strongly and specifically bind its complimentary intended target and remain bound for a long time.

Assessment of Safety of Nanoligomer Treatment in Mice. The safety of SBCoV207 was evaluated in a murine model. Mice were administered with SBCoV207 either intranasally (IN), intraperitoneally (IP) via injection, or intravenously (IV) via tail vein injection, and then observed for 5 days before being euthanized (Figure 2A). Collected samples were then analyzed for any abnormalities compared to phosphate-buffered saline (PBS)-treated control groups.

Eight week-old female BALB/c mice were divided into groups of five. Increasing doses of SBCoV207 were tested sequentially, starting at 1 mg/kg, then on to 2, 5, and finally 10 mg/kg. Note that these doses are 10 to 100 times higher than doses that showed efficacy in lowering viral titers in hamsters.[41] Mice treated via IP injection were only tested at 10 mg/kg SBCoV207. Mouse weight was monitored daily (Figures 2B−F, S2B,C, and S3B−F), along with checking for behavioral changes or signs of distress. On the 5th day, mice were euthanized by cervical dislocation for IN treated mice and carbon dioxide (CO_2) exposure for all other mice. Cervical dislocation allowed for the preservation of lung tissue without risking damage from carbon dioxide exposure or any other respiratory euthanasia method. Therefore, this method was used for IN-treated mice, while the more standard CO_2 euthanasia was used for remaining mice to limit pain and distress. Blood and urine were collected, and serum was separated from whole blood for enzyme-linked immunosorbent assays (ELISAs) (Table S2 and Figure S4). Brain, lung,

kidney, liver, spleen, and lymph tissue were collected and either drop-fixed for histology analysis or frozen for later homogenization and analysis via mass spectrometry. Additionally, colon tissue was collected from intraperitoneally treated mice.

In all groups, mice showed no change in weight, with every mouse losing no more than 1 g of bodyweight on any one day of the study, compared to day zero (Figures 2B−F, S2B,C, and S3B−F). This falls within the measurement error of the scale used. Mice did not appear outwardly distressed and continued to eat and drink as usual.

Histology and Pathology. Formalin-fixed liver, spleen, kidney, and lung samples from mice that received either 5 mg/kg of SBCoV207, 10 mg/kg of SBCoV207, or PBS control were processed for histology to assess tissue health (Figures 3, S5, and S6). In IN-treated mice, alveolar hemorrhage in the lung was observed in similar severity compared to the PBS control lungs (Figure 3D−G). Hemorrhage into alveoli and bronchioles, accompanied by bright eosinophilic proteinaceous material, were observed; hemorrhage was generally seen in a hilar distribution or surrounding airway/vascular structures. This finding was considered peracute as neither increased alveolar macrophages, erythrophagocytosis, nor hemosiderin pigment was observed. Mice that did not have blood collected via submandibular bleed prior to euthanasia showed no signs of alveolar hemorrhage (Figure S7); as such, the bleeding was attributed to the blood collection method rather than due to SBCoV207 administration 5 days prior. Hemorrhaging in lungs was similarly observed in IP and IV administered mice (Figures S5 and S6), in this case due to CO_2 euthanasia.

In the liver, minimal subacute inflammation was observed in nearly all mice; incidence and severity were similar across control and SBCoV207-treated groups and all administration routes (Figure 3A−C). While livers from mice treated with 10 mg/kg of SBCoV207 intranasally (Figure 3D) showed a statistically significant difference in liver histological severity grade compared to the control group, the grades across all assessed livers were low, indicating that this result does not reflect a change in liver morphology due to the Nanoligomer treatment. Inflammatory cells typically consisted of neutrophils, macrophages, and lymphocytes admixed with few necrotic hepatocytes. Small, randomly distributed inflammatory foci in the liver are typically considered secondary to decreased barrier function in the GI tract and result from showering of bacteria through the biliary tract and/or blood stream. This is a common background finding in mice[61] and is considered unassociated with SBCoV207 administration. There were no histologic findings in the spleen or kidneys of the control or SBCoV207-treated animals (Figure 3A−C).

Absence of Inflammatory Response. TNF-α, IL-6, and albumin levels were measured in mouse serum (Table S2 and Figure S4). TNF-α and IL-6 are indicators of inflammation and cytokine response. Albumin levels reflect liver and kidney health.[62,63] All three of these parameters were normal in all tested mice. In healthy mice, both TNF-α and IL-6 levels remain below the level of detection of the ELISA. This was the case for all tested samples, with measured absorbance falling below the range of the assay calibration curve (Figure S8). Average albumin levels were lower than the control group for IN groups (Figure S4A), but due to the wider range in levels seen in the control group, the difference was not statistically significant ($p > 0.23$). Albumin levels in IP and IV mice were also not statistically different from control groups (Figure
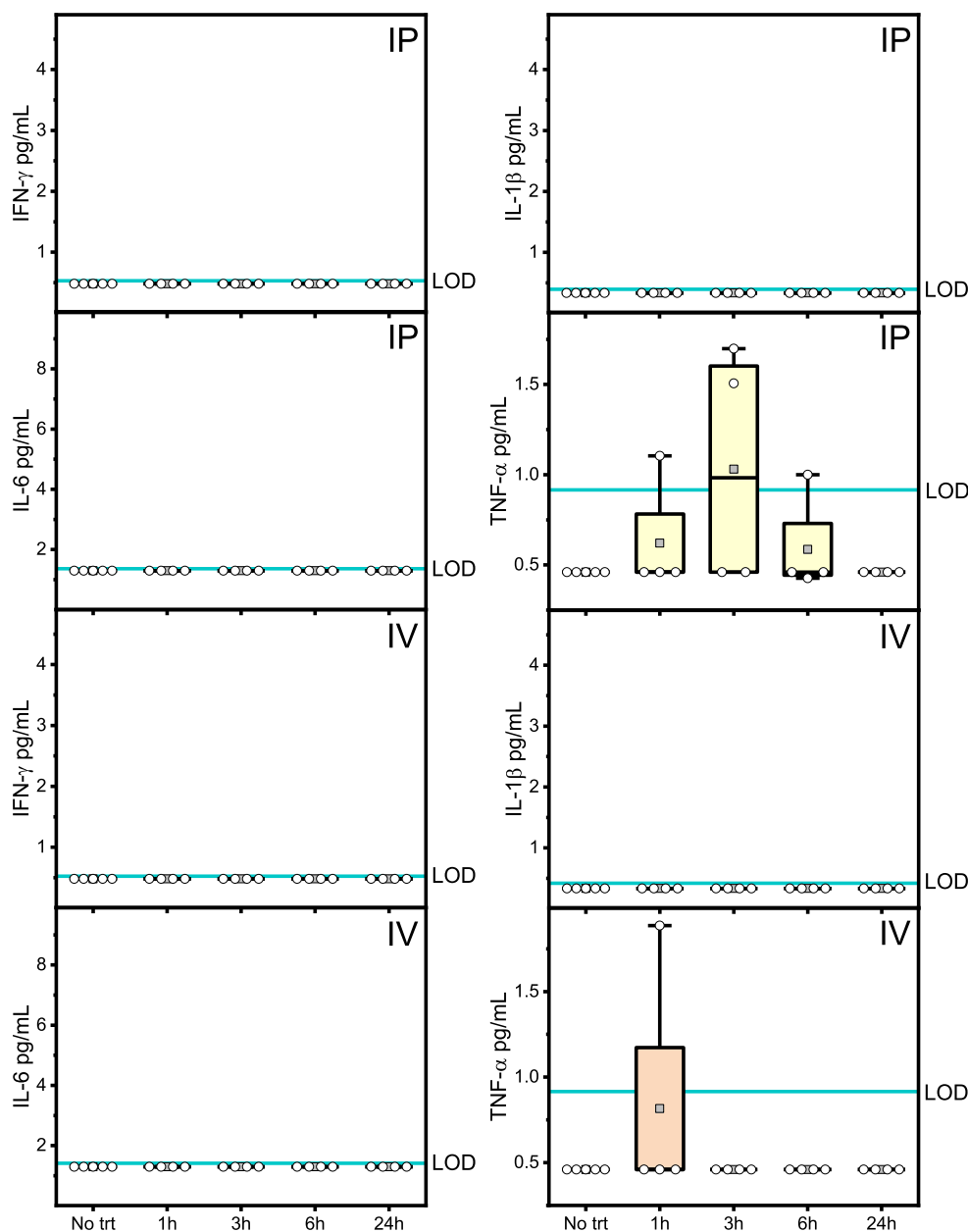
Figure 4. 36-cytokine/chemokine panel performed on serum samples from mice treated with SBCoV207 via intraperitoneal (IP) or intravenous (IV) injection showed key cytokines below the LOD of the assay, namely, IFN-γ, IL-1β, IL-6, and TNF-α. The LOD is represented with a blue line. All groups showed $p > 0.05$ compared to the PBS control group. $n = 5$ for the no treatment control group, otherwise $n = 4$.

S4B,C, $p > 0.07$ and 0.25, respectively). This therefore indicates lack of inflammation and hepatic and renal health.

Serum from mice treated with IP- and IV-injected SBCoV207, and then euthanized 1, 3, 6, or 24 h after administration, was tested in a 36-plex cytokine/chemokine panel (Figures S9–S14). Most cytokines and chemokines did not show levels significantly different from the control group. Importantly, representative markers of inflammation, namely, IFN-γ, IL-1β, IL-6, and TNF-α, were found to be below the limit of detection (LOD) or statistically similar to no treatment (Figure 4). The low IFN-γ levels specifically indicate that a T-cell response to SBCoV207 likely did not occur. IL-1β, a cytokine responsible for fever production and a marker of activated macrophages, was also below LOD (Figure 4). TNF-α and IL-6 levels, tested by single-cytokine ELISAs, in all serum samples remained below the level of detection of the

ELISA between 1 and 24 h after SBCoV207 administration (Table S3). This is in line with results from the 36-plex panel (Figure 4) and the 5-day study (Table S2) and further confirms no notable acute immune response to SBCoV207.

Biodistribution of SBCoV207 in the Murine Body. The biodistribution of SBCoV207 was examined through a 24 h kinetic study. 8 week-old female BALB/c mice, in groups of five, were treated with SBCoV207 and then euthanized at 1, 3, 6, or 24 h after treatment. Samples of whole blood, urine, brain, lung, kidney, liver, spleen, and lymph tissue were collected for analysis via mass spectrometry. Colon tissue was collected from IP- and IV-treated mice. Blood serum was also collected for ELISAs (Figures 4 and S9–S14).

Homogenates of lung, brain, lymph, kidney, spleen, liver, and colon and volumes of whole blood and urine were assessed for the presence of Nanoligomers using inductively coupled
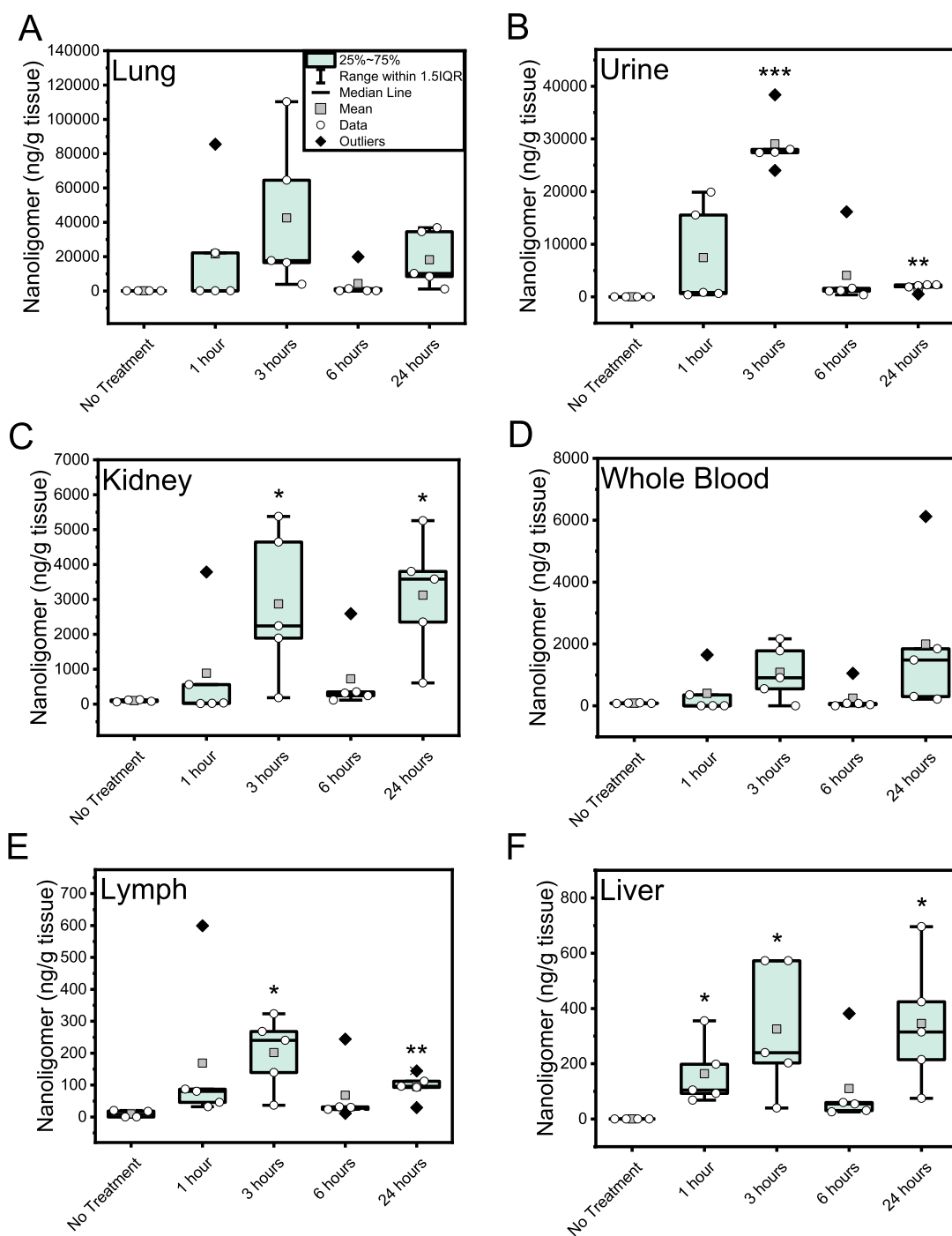
Figure 5. SBCoV207 biodistribution after intranasal administration showed SBCoV207 (shown as nanograms per gram of tissue) reaching the lungs (A), being cleared by the renal system (C), and excreted by the urinary system (B). SBCoV207 was circulated in the whole blood (D), and SBCoV207 was detected in the lymph (E) and liver (F) tissue. p-value indicated by * < 0.05, ** < 0.01, *** < 0.001, otherwise $p > 0.05$. $n = 4$ for the no treatment control group, otherwise $n = 5$.

plasma mass spectrometry (ICP−MS) (Figures 5 and S15−S18). Parts per billion (ppb) of detected gold due to Nanoligomers was then converted into nanograms of Nanoligomer per gram of tissue (ng/g tissue). Highest levels of Nanoligomers were detected in the urine, lungs, kidneys, and whole blood (Figure 5A−D).

Intranasal Biodistribution. The lung, the most immediate site for biodistribution in IN administered drugs, showed high levels of SBCoV207, in the range of 15−18,000 ng/g organ, or 1−4 μM, within the first 3 h after administration (Figure 5A).

Amount of SBCoV207 peaked at 3 h. While the variability in the amount of SBCoV207 reaching the lungs via IN administration was clear (Figure S16), the PK data showed much higher concentrations (>IC90, Figures 1C and 6A) in lungs compared to IP (Figure 6B) and IV (Figure 6C, >IC50), including the lowest t_{max} values (3 h for IN, compared to 6 h for IP and IV routes), making it the route of administration of choice for lung delivery as a SARS-CoV-2 antiviral.

SBCoV207 was cleared quickly through the renal system and through urinary excretion (Figures 5 and 7) but showed much
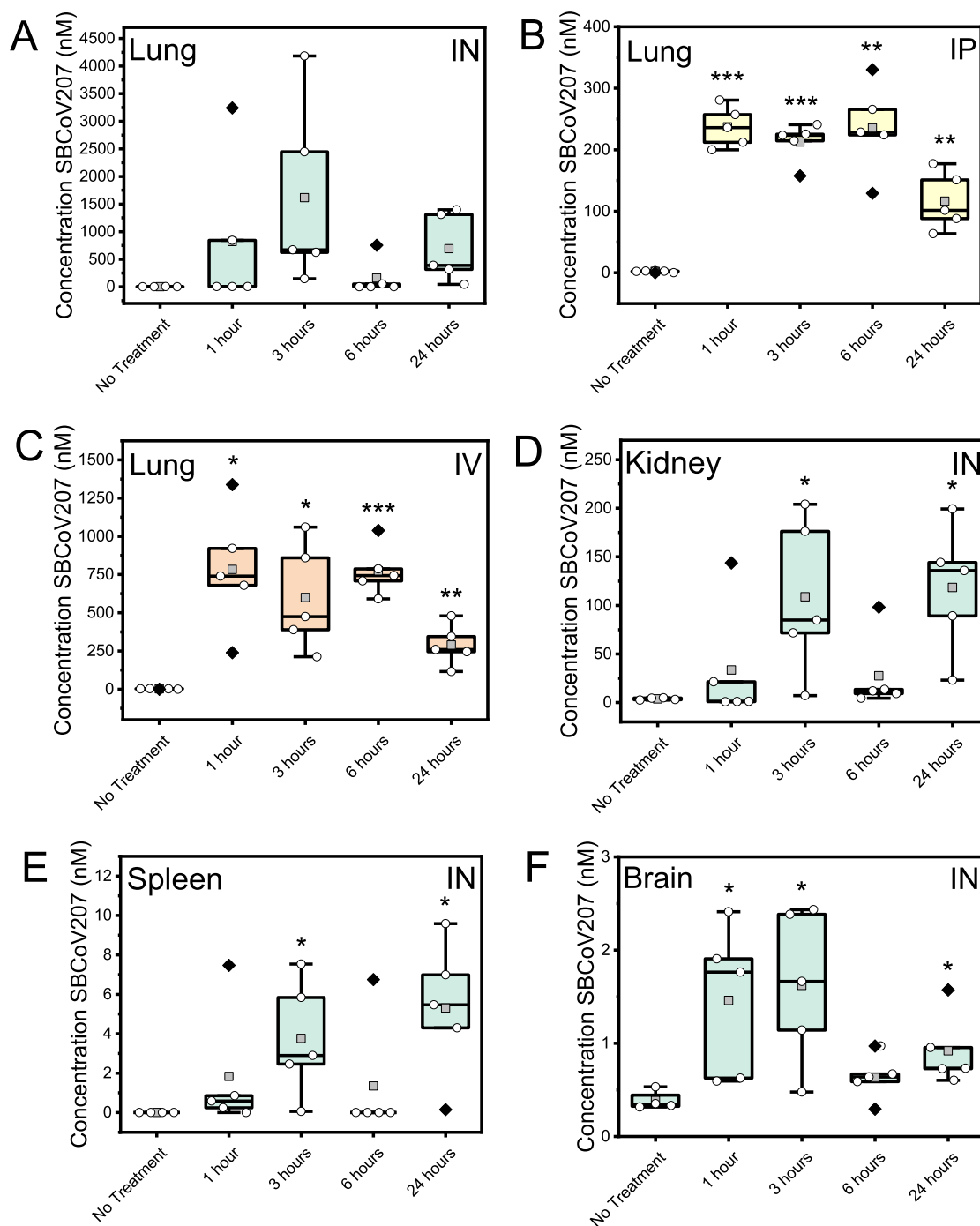
Figure 6. PK data in lungs after (A) intranasal, (B) intraperitoneal, and (C) intravenous administration. While SBCoV207 has a low K_D value (48.11 nM, Figure 1D), based on in vitro antiviral efficacy data (IC_{50} = 500 nM, Figure 1C), the target concentration is achieved using IN ($>IC_{90}$) and IV ($>IC_{50}$) routes of administration of 10 mg/kg SBCoV207. We note that due to inconsistent amounts of SBCoV207 reaching the lungs via IN administration, there is much larger deviation in IN PK data than IP and IV routes. SBCoV207 is cleared by the renal system (D) and excreted by the urinary system. Besides the lungs, SBCoV207 concentrations were lower in other organs such as the spleen (E) and brain (F). p-value indicated by * < 0.05, ** < 0.01, *** < 0.001, otherwise p > 0.05. n = 4 for the IN no treatment control group, otherwise n = 5.

lower concentration in other organs such as the spleen and brain (Figures 8 and S15). Levels of SBCoV207 in the kidneys rose over time but all remained below 5400 ng/g tissue (Figure 5C). With the exception of the 6 h group, measured levels were significantly higher than the control group (p < 0.05). In the urine, levels of Nanoligomer were highest at 3 h after administration (p < 0.001) and dropped over time (Figure 5B). By 24 h, almost no SBCoV207 was detected in urine,

though it remained statistically different from the control group (p < 0.01). This indicates an initial rapid clearance through urinary excretion, with SBCoV207 quickly passing through the kidney. Some Nanoligomer seems to have been transported into the lymphatic system. The lymphatic system often funnels compounds into the renal system. Overall SBCoV207 levels in the lymph were low, at less than 600 ng/g tissue, but levels were higher at 1 and 3 h after administration
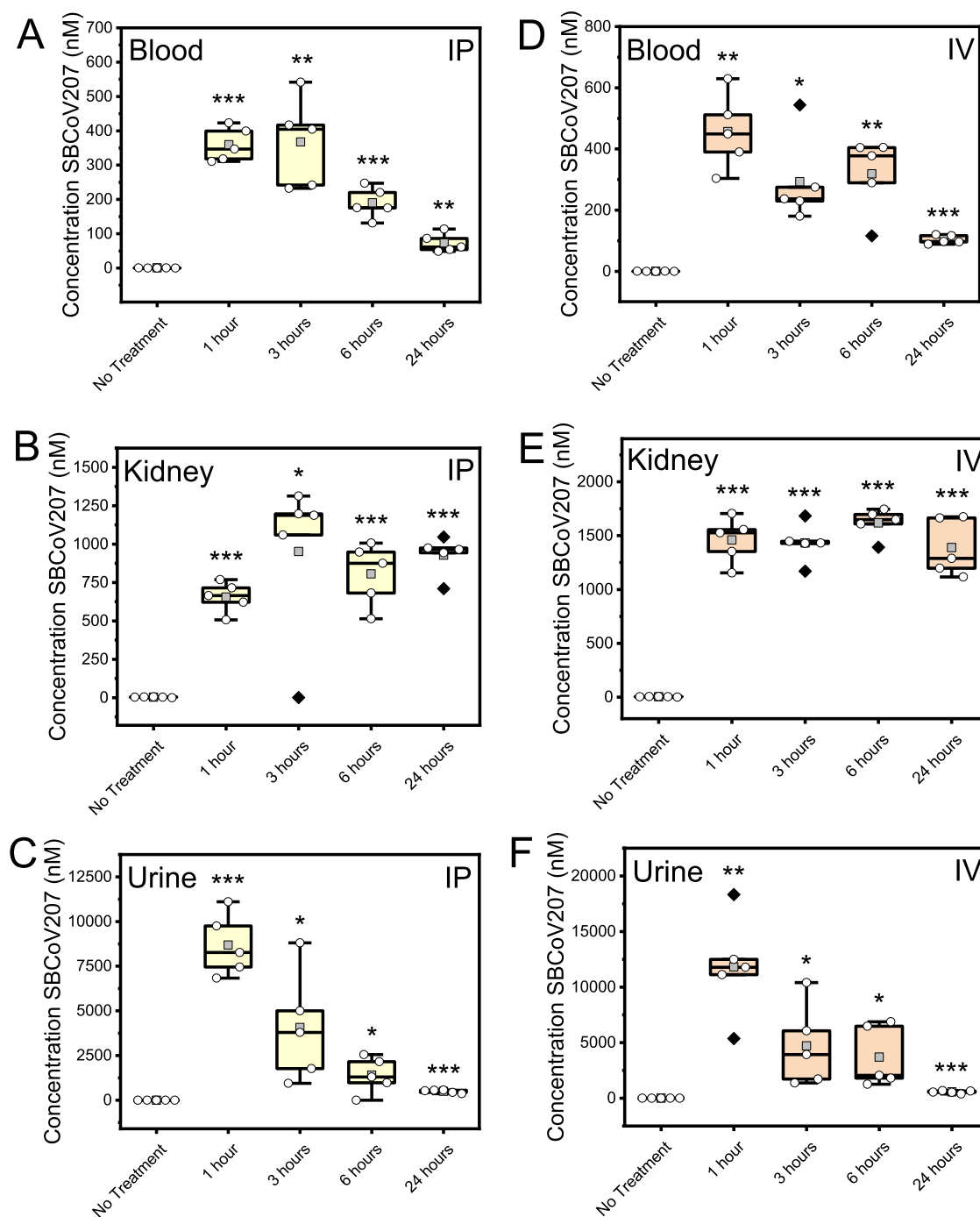
Figure 7. (A−C) Intraperitoneal and (D−F) intravenous PK and biodistribution data for blood, kidney, and urine. SBCoV207 amounts are given in nM. p-value indicated by * < 0.05, ** < 0.01, *** < 0.001, otherwise p > 0.05. n = 5 for each time point.

and decreased over time (Figure 5E, p < 0.05). Some SBCoV207 was also transported in the whole blood, though all but one sample showed less than 2200 ng/g blood (Figure 5D). The outlier showing 6100 ng/g blood at 24 h was unexpected but may indicate that the compound could still be circulating in the body hours after administration. The effects of the variability in IN administration are noticeable in the consistently lower levels of SBCoV207 measured in only the 6 h group (Figure S16).

The amount of SBCoV207 found in the liver decreased at the 6 h time point but was otherwise significantly different from the control group (Figure 5F, p < 0.05). The lower levels

in the 6 h group are likely due to inconsistent administration for the group rather than an effect of biodistribution of SBCoV207, as these mice also showed lower levels of SBCoV207 in all organs (Figure S16). Levels in spleen rose slightly over time but all remained below 260 ng/g tissue (Figure S15A). Brain levels were below 65 ng/g tissue for all groups (Figure S15B).

Intraperitoneal Biodistribution. Biodistribution was similarly assessed in mice administered 10 mg/kg of SBCoV207 via IP injection and then euthanized at 1, 3, 6, or 24 h after injection. Levels of SBCoV207 present in organs indicate that this administration method has lower biodis-
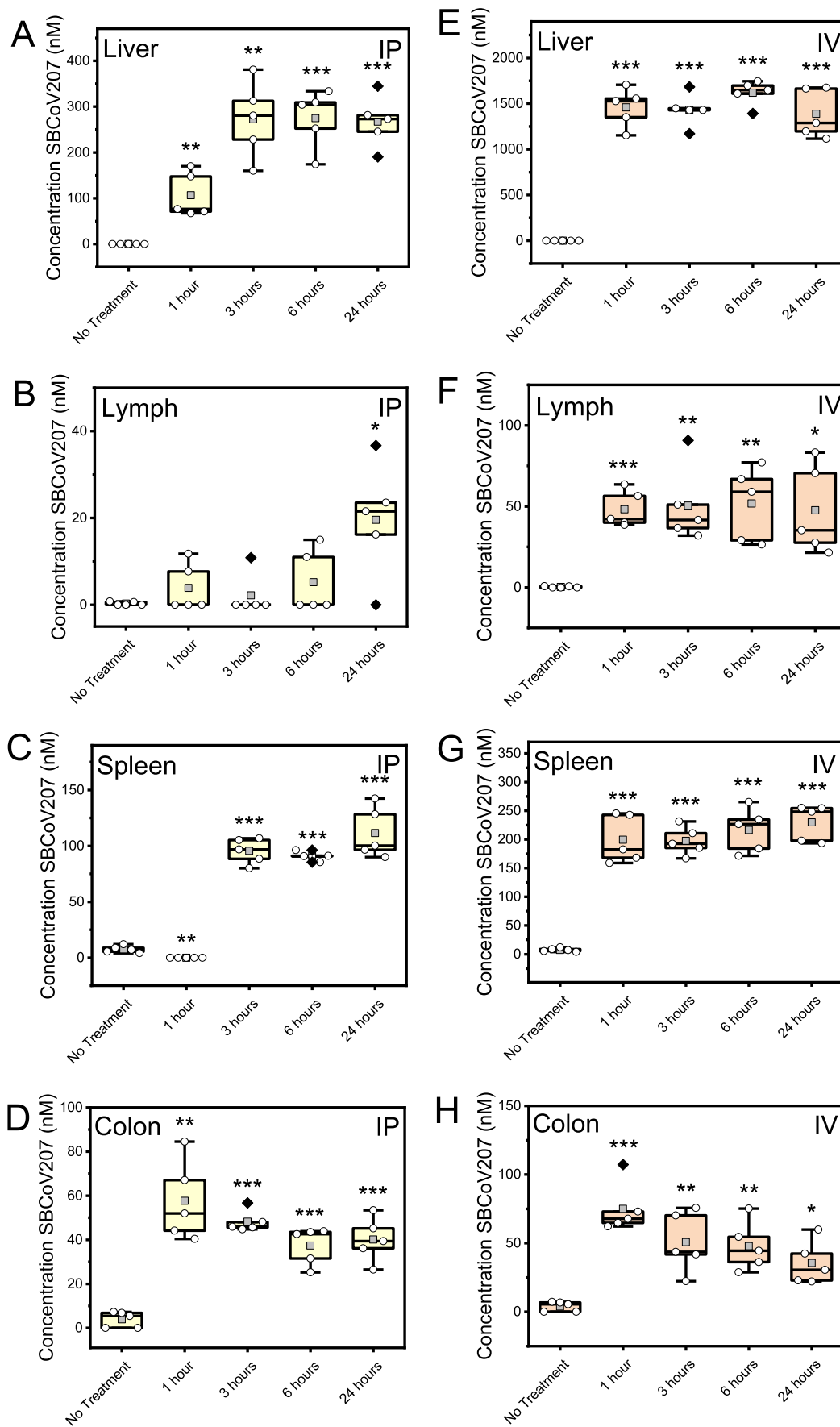
Figure 8. (A−D) Intraperitoneal and (E−H) intravenous PK and biodistribution data for liver, lymph, spleen, and colon. SBCoV207 amounts are given in nM. p-value indicated by * < 0.05, ** < 0.01, *** < 0.001, otherwise $p > 0.05$. $n = 5$ for each time point.
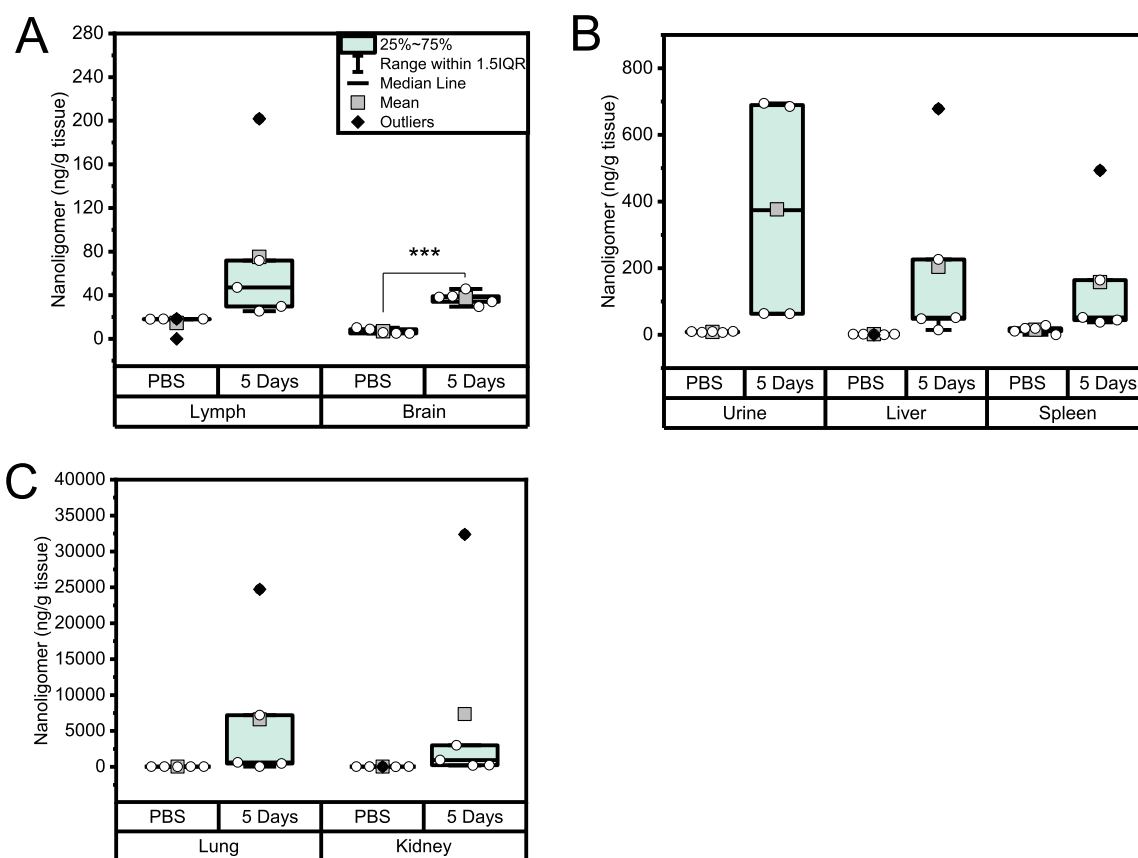
Figure 9. SBCoV207 biodistribution 5 days after 10 mg/kg intranasal administration showed SBCoV207 largely no longer present in the lymph or brain tissue (A), present to a moderate degree only in some mice in urine, liver, and spleen (B), and still present at higher concentrations in only two and one mouse in lung and kidney, respectively (C). p-value indicated by * < 0.05, ** < 0.01, *** < 0.001, otherwise $p > 0.05$. $n = 5$ for each treatment group.

tribution of treatment to the lungs compared to IN (Figure S17A), with the amount of SBCoV207 present being below 8000 ng/g lung even at early time points. By 24 h after injection, all mice showed less than 5000 ng/g lung. Levels in urine (Figure S17B) were nearly an order of magnitude higher compared to IN administration, with rapid excretion within the first 3 h. Higher SBCoV207 concentrations were also seen in kidneys and blood (Figure S17C,D). The nearly 10,000 ng/g average seen in the blood indicates that the SBCoV207 quickly reached systemic circulation and reached other organs via the bloodstream. However, levels in the blood dropped off with time. Levels in the liver were over a magnitude higher compared to IN administration (Figure S17F). SBCoV207 thus passed into the portal vein. This wide distribution also likely caused the relative increase in the presence of SBCoV207 in the spleen over time (Figure S17G). The amount of SBCoV207 measured in kidneys, liver, and spleen remained mostly unchanged from 3 to 24 h after injection. Levels of SBCoV207 in the lymph nodes (Figure S17E) were comparable to IN administration. Colon showed some amount of SBCoV207 as well (Figure S17H). SBCoV207 was detected in the brain within an hour after injection (Figure S17I).

Intravenous Biodistribution. An identical experiment was performed to assess biodistribution after intravenous injection. SBCoV207 was injected via the lateral tail vein of mice. Biodistribution to lung was much improved in IV-treated mice (Figure S18A) compared to IP-treated groups, with levels of SBCoV207 only slightly decreased compared to IN

administration. Similar to IP injection, urinary excretion was rapid and effective (Figure S18B). While SBCoV207 levels in the kidneys were slightly elevated compared to IP treatment (Figure S18C), amounts in the circulation were comparable (Figure S18D). Between all three administration routes, IV injection showed the highest levels in lymph (Figure S18E), liver (Figure S18F), and spleen (Figure S18G). Once again, levels in the kidneys, liver, and spleen remained largely consistent over the course of the 24 h. SBCoV207 levels in colon were similar to IP administration (Figure S18H) and no SBCoV207 was detected in the brain (Figure S18I).

Regardless of administration route, mice did not show signs of toxicity at any point from 1 h to 5 days after SBCoV207 administration. SBCoV207 was largely cleared via urinary excretion within a few hours of administration, and accumulation in organs was low by 5 days post-administration. The toxicity studies performed and parameters measured indicate that SBCoV207 remains a safe and promising candidate for a novel antiviral against SARS-CoV-2.

Rapid Clearance and Bioavailability of SBCoV207. The PKs of SBCoV207 were examined through a 24 h kinetic study by converting moles of SBCoV207 in different organ tissues to concentrations (mole/volume) by using tissue densities (Figures 6−8).[64] Furthermore, the kinetic biodistribution of SBCoV207 was estimated in different organs by using their measured SBCoV207 amounts in different organ tissues, and respective estimates of organ masses for 8 week old female BALB/c mice to calculate the fraction (% of total

SBCoV207 injected in each animal) of SBCoV207 in different murine organs (Figures S19 and S20).

Data indicate renal clearance (Figures 7 and S19) through both IP and IV routes of administration. Using PK data for IP (Figure 7A) and IV (Figure 7D) in blood, and drawing a curve using average values, we estimated the area under curve (AUC) and bioavailability (F) for IP administration (F = AUC IP/AUC IV)[65] for the single dose as ~0.7. This value is comparable to other small molecule therapies. High uncertainty in estimating urine content led to large variability in determining biodistribution of SBCoV207 in urine, especially at early time points (Figure 7C,F). However, rapid clearance of SBCoV207 and achievement of steady state concentration (t_{max} < 1 h for IV administration) indicates rapid biodistribution and clearance of SBCoV207. T_{max} for IP administration was ~3 h (Figures 7 and 8).

While biodistribution to various organs, including the liver, lymph, spleen, and colon, was high (Figures 8 and S20), no accumulation in these organs was observed. Concentrations of SBCoV207 in these organs generally did not increase after the first 3 h after administration, whether through IP or IV injection. The steady-state concentration achieved was well above the K_D of SBCoV207 in the liver and spleen.

IV administration showed rapid transport of SBCoV207 to the lymph nodes, with concentrations of approximately 50 nM and about 1% of administered SBCoV207 reaching the lymph nodes within 11 h (Figure 8B,F). By comparison, the IP route lagged in delivery to the lymphatic system, and SBCoV207 concentration rose even after 24 h, reaching 20 nM with about 0.25% of total SBCoV207 delivered at 24 h.

Biodistribution of SBCoV207 after 5 Days. Levels of SBCoV207 were also assessed in organs of mice treated with SBCoV207 on day 0 and euthanized on day 5 (Figure 9). Five days post-treatment, SBCoV207 was present in amounts of less than 200 ng/g tissue in the lymph and brain (Figure 9A). Urine, liver, and spleen showed SBCoV207 remaining only in some mice of a magnitude of 500−700 ng/g tissue, while others showed considerably lower remaining SBCoV207, comparable to the control group (Figure 9B). Two mice showed relatively high levels of SBCoV207 remaining in lung, while a separate mouse showed SBCoV207 in the kidneys (Figure 9C). This highlights the stochastic delivery of SBCoV207 to the lungs via intranasal administration. However, due to other mice showing low levels in all organs comparable to the control group, only SBCoV207 levels in brain showed statistical significance between groups (p = 0.0001).

■ DISCUSSION

COVID-19 has proven to be a deadly disease with global implications. In many cases of severe COVID-19, host hyper-responses such as the cytokine storm syndrome, triggered by the virus,[4] can lead to fatal outcomes. SARS-CoV-2 is hypothesized to increase the innate immune response while dampening adaptive immune response.[4,66] Nonspecific immune response, including upregulation of cytokines, continues in patients in the absence of adequate counts of CD4 and CD8 T-cells to target the virus for clearance.[4] Thus, rampant but nonspecific host response may result in more permanent or long-lasting effects on the patient.[67] New compounds to suppress harmful host response in patients infected with SARS-CoV-2 could drastically alter survival rates and improve long-term prognosis, especially in regions with low vaccination rates

or high incidence of more infectious variant strains. Here, we test the material safety of SBCoV207 Nanoligomers, which could attenuate severe host immune response to infection, a common cause of death among COVID-19 patients.

Nanoligomers are ideal molecules for the specific targeting of nucleic acids such as miRNAs.[23,41] We have shown previously that the PNAs show high specificity to target sequences.[68,69] This allows for versatility in target selection and prevention of off-target binding. PNAs are highly stable in vivo and demonstrate strong binding to nucleic acid targets.[13,15] The Nanoligomers have also shown efficacy against SARS-CoV-2 both in vitro (Figure 1C) and in vivo, without causing toxic responses to the host cells or animals.[41] Nanoligomers can thus be used to modulate levels of circulating miRNA in infected humans, including binding miRNAs such as miR-2392 that are linked to more severe cases of COVID-19.[41]

The Nanoligomers also provide an attractive alternative to other antisense therapeutics due to their small size and ease of transport without requiring encapsulation. Particles as small as the 15-base PNA sequence conjugated to a nanoparticle can traverse across cell membranes without relying on endocytosis, thereby circumventing the necessary step of endosomal escape that other ASO and their drug delivery systems must overcome.[27,70,71] Furthermore, past lipid encapsulation methods have achieved low encapsulation efficiencies of less than 10%,[70,72] which has since improved to 70% or higher but can still pose challenges.[72,73] Variation in the degree of association between the lipid and payload and unknown aspects of the structure[74] highlight the work still to be done in optimizing lipid encapsulation methods. The use of Nanoligomers avoids concerns over non-uniform size, complex formulation, and difficulties with scaling up production seen in platforms such as liposomes and lipid nanoparticles (LNPs).[27,72,74−76] Any protein adsorption that may occur would not increase the Nanoligomer size drastically, allowing for the observed rapid renal clearance. This reduces side effects to the treatment and demonstrates that Nanoligomers face fewer obstacles around tolerability and biocompatibility compared to lipid systems.[26]

SBCoV207 did not cause significant toxicity in mice during the 5 days they were observed after SBCoV207 administration, whether administered via IN, IP, or IV routes. Mouse weight remained within a normal and healthy range (Figures 2, S2, and S3). No activation of the innate immune system, which may occur with CPP-conjugated PNA and with siRNA,[25,28,30,46] was observed as a result of Nanoligomer treatment (Figure 4). Our Nanoligomers circumvent the issue of undesired immune responses caused by CPPs[25,46] by using biocompatible gold nanoparticles.[47,77] Serum parameters, namely, TNF-α, IL-6, and albumin, showed no indicators of inflammation, immune response, or damage to the hepatic or renal systems (Figure S4 and Table S2). This is especially promising in light of siRNA technologies that have induced elevated TNF-α and IL-6 levels.[28,29]

In a 36-plex cytokine/chemokine panel, four molecules showed a statistically significant increase in serum levels for IP-treated mice only (Figure S9). None of these increases persisted to 24 h after SBCoV207 administration. It is likely that these increases, which were not observed in the IV-treated mice, were due to the invasive IP injection rather than the presence of SBCoV207. GRO-α specifically is commonly associated with tissue injury.[78] It is worth noting that while the 1 h group serum differed significantly from control, ELISA kit datasheets report GRO-α levels of up to 255 pg/mL in normal

and healthy mice (Mouse CXCL1 Quantikine ELISA, R&D Systems, Minneapolis, MN), an order of magnitude above values observed here.

While other ASO and drug delivery methods have been linked to elevated levels of IFN-α and IFN-γ[26,28,29] and require modification to circumvent this,[30,31] we observed no such effects with SBCoV207. IFN-α levels (Figures S10 and S13) and IFN-γ levels (Figure 4) remained below LOD. IL-18, which was elevated only in IP-treated mice, enhances IFN-γ production,[79] but as IFN-γ levels remained below LOD (Figure 4), the likelihood of a full T-cell response to SBCoV207 is low. IL-18 also acts upstream of GM-CSF and IL-6,[80] but levels of both remained low as well (Figures 4, S10, and S13). Reports of serum from healthy mice show measurements below 200 pg/mL is considered normal for IL-18,[81] further supporting a lack of immune response to SBCoV207. These results were expected, considering the lack of immunogenicity from naked PNA[25] and the biocompatibility of gold.[82]

Nanoligomer levels were highest in the lung when administered intranasally (Figure 5A), which was in line with expectations. High drug concentrations at the infection site allow for improved treatment outcomes, as a lower dose can be used to achieve similar results to an IV injection. This minimizes side effects elsewhere in the body. However, levels of SBCoV207 detected in the lungs were highly variable. While IN administration is technically very simple and more applicable to human administration methods,[54−56] future studies using oral pharyngeal aspiration may allow for higher consistency in administration volume between mice.[83] Differences in the physiology of human and mouse respiratory systems and oral structure[84,85] complicate the direct translation of mouse IN administration to human IN administration. Importantly, mice are obligate nasal breathers and therefore do not breathe through their mouths.[84] IN delivery via droplets of fluid placed on the nostrils may result in some compound externally leaking down the snout to the mouth and being swallowed instead of breathed in, resulting in variability of compound concentration in the lungs. Some mice showed higher levels of SBCoV207 across all organs compared to mice within the same treatment group (Figure S16), further indicating that IN administration results in differences in the concentration of compound that actually reaches the lung.

SBCoV207 appeared to be cleared by the renal system, based on levels detected in the liver, and excreted via the urine (Figure 5B,C). In IP- and to some degree IV-treated mice, SBCoV207 presence in the urine far exceeded the presence in the lungs and other organs (Figures 6−8). A large portion of the SBCoV207 dose was therefore rapidly and efficiently excreted. Though clearance and elimination that occur within minutes of administration pose a concern for inadequate compound circulation through the body, the Nanoligomer appears to remain in the body for hours, allowing for therapeutic activity. While a measurement of SBCoV207 levels immediately after IV injection would be necessary to assess the half-life of SBCoV207, most of the administered SBCoV207 was still detectable in the urine at 1 h after injection (Figure S19C,F), indicating that SBCoV207 is not eliminated within the first minutes after administration. Extremely rapid half-lives and elimination have been observed with lipid-encapsulated ASOs, especially those utilizing cationic lipids,[72] but in the case of SBCoV207, the compound continues to be detected in the urine and blood hours after administration.

Levels of SBCoV207 in the blood of mice were low compared to lungs and urine (Figure 5D), but the bioavailability was favorable and comparable to small-molecule drugs at about 0.7. Higher levels of SBCoV207 in the 1 and 3 h IN groups compared to 6 and 24 h suggest that SBCoV207 crosses the epithelial barrier to enter the bloodstream within the first few hours, allowing for this favorable bioavailability. The total fraction of SBCoV207 observed in the blood was comparable to that seen in the lungs for IP-administered mice (Figures 6B and S19), but was slightly lower than in the lungs for IV-injected mice (Figures 6C and S19). At about 10−20% of injected dose residing in the blood 1 h after administration (Figure S19A,D), SBCoV207 demonstrated considerably improved bioavailability compared to, for example, fluorescently labeled siRNA with or without silica nanoparticles, at 5% in 1 h and 1% in 20 min, respectively.[86,87]

Biodistribution of SBCoV207 generally followed expectations for oligonucleotides. Neutral compounds such as PNAs, morpholinos, and unmodified siRNA typically demonstrate rapid clearance from circulation via urinary excretion,[88−90] as observed here. While the kidney is therefore the primary organ of biodistribution for most administration types, intranasal administration temporarily increases the biodistribution of SBCoV207 to the typical infection site, the lungs. Most ASO show rapid accumulation in first pass organs such as the liver.[88,90−95] For example, PK and biodistribution data show ∼50−100 μg/g ASO in liver using 3−4 mg/kg IV injection,[88] accounting for more than 70% of administered ASO. While that provides delivery of the ASO to the liver, kidneys, and adipocytes, other organs can have very limited biodistribution, making them hard to use for antiviral and systemic applications such as downregulating circulating miRNA, including miR-2392. Even in the use of LNPs for oligonucleotide delivery, the ASOs easily reach the lung and spleen but show limited biodistribution to other organs without significant modification.[27] While liver accumulation is reduced (∼100 nM), the PK data indicates low (<100 to <10 nM in non-first-pass organs) bioavailability of ASO in most organs.[86,96,97] Data from both IP (Figure 8A) and IV (Figure 8E) injected mice do not show accumulation in the liver or in other first-pass organs such as the kidney and spleen (Figure 7B,E and 8C,G). High bioavailability (0.7) to all organs, rapid biodistribution, and lack of accumulation in first-pass organs such as the liver show favorable "small-molecule"-like delivery of Nanoligomers, with high specificity and low K_D (48 nM) similar to recombinant proteins and biologics. The high concentration (Figures 6−8) observed in vivo, well above the K_D values, supports SBCoV207 as a potential systemic antiviral against SARS-CoV-2, although further PK/PD and detailed efficacy studies need to be done to prove pre-clinical efficacy. This relatively uniform biodistribution simplifies the delivery of Nanoligomers, especially if considering applications beyond respiratory infections.

The lymph nodes of some IN-treated mice showed SBCoV207 concentrations higher than the control group (Figure 5E). IV- and IP-treated groups also showed the presence of SBCoV207 in the lymph (Figure 8B,F). Comparison with other ASO shows very limited or undetectable biodistribution to the lymph nodes using other platforms,[86,88,90−95,98,99] while Nanoligomers were present in concentrations above the K_D for some IV-treated mice (Figure 8F). This provides unique advantages for Nanoligomers in targeting the innate immune system for antiviral applications.

Levels of SBCoV207 in the brain were very low compared to other organs but significantly different from the control group (Figure S15B). We note that the Nanoligomers can cross the blood–brain barrier, unlike other ASO,[88,90−95] siRNA,[86,90,98,99] and other modified nucleotide technologies, which must rely on highly invasive intracerebral and intrathecal direct injections.[88,100] The Nanoligomers thus offer a unique advantage in delivering antivirals and other therapies for infectious and non-infectious targets in the brain. The high specificity of PNA could allow for efficacy against a variety of diseases localized in the brain even at low concentrations, and applications of PNA in nerve repair, where currently there is progress in nucleic acid-based therapeutics,[101] could also be explored. However, with SBCoV207, the low concentrations observed in the brain using the IN and IV routes, which remained well below the K_D of 48 nM (Figure 6F), require that other routes of administration (IP or otherwise) and specific brain-targeted sequences should be tested to evaluate the efficacy of Nanoligomer delivery for this application.

As SBCoV207 targets a human host factor, miR-2392, off-target binding in mice is not expected. Mice do not produce miR-2392 naturally, though homologous miRNA may exist in dog, cat, and ferret genomes.[41] SBCoV207 would therefore first require toxicity and efficacy testing in dog or ferret, then non-human primates, before more intensive safety testing in human trials to ensure no ill effects due to specific binding to the miRNA target. However, these studies do confirm the lack of material toxicity from Nanoligomers, as well as indicate the expected biodistribution in humans. Furthermore, after 5 days, IN-administered SBCoV207 was largely cleared from the body, with only isolated instances of SBCoV207 detected in lung and kidney (Figure 9). Effective clearance ensures minimal risk of toxicity due to the long-term accumulation of SBCoV207 in the organs. This, combined with the lack of toxicity observed in hamsters and the trend of decreasing viral load in SARS-CoV-2 infected hamsters at even suboptimal doses of 0.13 mg/kg,[41] demonstrates the potential of SBCoV207 as an effective treatment for COVID-19.

Efficacy testing in infected animal models at concentrations of 10 mg/kg or higher would elucidate the therapeutic window of the compound, which has already been shown to be much wider than first tested in hamsters.[41] Multiple-dosing studies would also provide a more comprehensive analysis of the PKs, pharmacodynamics, and clearance rates of the Nanoligomers. Due to their sequence-specific nature, Nanoligomers could also easily be adapted to target other miRNA associated with severe disease state, making them ideal anti-inflammatories. Several miRNA have been linked to severe reactions to coronavirus infections.[32,36] The adaptability of the Nanoligomer design would allow for a variety of targets. This could assuage concerns around virus variants or emerging new viruses that result in different miRNA expression profiles within the infected host. Furthermore, studies are currently being conducted on Nanoligomers designed to directly target the viral genome. It is plausible that a combination of Nano-ligomers targeting various miRNA and viral genome sequences could be used to treat COVID-19 in a versatile and individualized way.

CONCLUSIONS

Effective antivirals for SARS-CoV-2 infections could drastically change the current landscape of pandemic treatment and control. The Nanoligomer treatment SBCoV207, which has

previously been shown to be an effective target for attenuating uncontrolled immune response to SARS-CoV-2 infection,[41] demonstrated no toxicity in mice at 10 mg/kg, whether administered via intranasal, intraperitoneal, or intravenous routes. Biodistribution analysis showed high biodistribution to the infection site, the lungs, especially with intranasal administration. The compound was renally cleared and excreted in the urine, with favorable biodistribution and bioavailability but little accumulation in other organs. This Nanoligomer treatment could potentially serve as a safe and effective treatment for severe cases of COVID-19, reducing the strain on hospitals and healthcare providers in areas with viral variant outbreaks or low vaccination rates, as well as offering a treatment strategy for countering future pandemics.

MATERIALS AND METHODS

Nanoligomer Design and Synthesis. Nanoligomers were designed and synthesized at Sachi Bioworks (Louisville, CO, USA) according to the methods described in McDonald et al.[41] After identification of the target miRNA,[41] a PNA sequence to target miR-2392 was designed. The human genome was scanned for the appearance of similar sequences elsewhere, which could result in off-target binding and side effects of taking the compound. Of six potential target sequences within the 20-nucleotide sequence of miR-2392, SBCoV207 was built from the sequence exhibiting the highest solubility and lowest incidence of self-complementing sequences and off-targets within the human genome.[41] Following the synthesis of the 15-base pair PNA molecules via solid-phase Fmoc chemistry on an Apex 396 and Vantage peptide synthesizer (AAPPTec, LLC), the PNA was incorporated into the Nanoligomer molecules. Nano-ligomers were purified by size-exclusion filtration. Conjugation and concentration were confirmed using absorbance measurements for detection of PNA and quantification nanoparticles.

SPR Measurements. A DNA oligomer containing 30 nucleotides of the human genome (hg38) with the miR-2392 binding target was biotinylated on the 5′ end (IDT). This oligomer probe was diluted to 5 μg/mL using 1× HBS-EP + buffer. This 1× HBS-EP + buffer was also used as running buffer during the SPR measurements. These oligomers were attached to a streptavidin-coated flow cell (Cytiva). The chip was first cleaned using a 10 μL injection of 20 mM NaOH/1 M NaCl solution. The probe was subsequently injected onto a flow cell of the chip. RU responses of 256 were observed, indicating probe binding to the chip. One flow cell on the chip was used as a reference; it was cleaned as described above but no probe was attached.

SPR measurements were carried out in accordance with previously established protocols.[60,102] The measurements were carried out on a Biacore 3000 instrument (Cytiva). Nanoligomer analyte was serially diluted using twofold dilutions from 20 to 1.25 μM. To measure association, 90 μL of Nanoligomer was run over the chip for 3 min at a flow rate of 30 μL/min. Dissociation was subsequently measured for 30 min. The chip surface was regenerated with a 10 μL injection of 20 mM NaOH + 1 M NaCl solution. Measurements for each concentration were repeated in triplicate. Data from the SPR measurements were analyzed using Scrubber 2.0 (BioLogic).

Virus Propagation and Plaque Assay. SARS-related coronavi-rus 2 (SARS-CoV-2), Isolate USA-WA1/2020 (NR-52281) was deposited by the Center for Disease Control and Prevention and obtained through BEI Resources, NIAID, NIH. SARS-CoV-2 was propagated in Vero E6 cells in DMEM supplemented with 2% fetal bovine serum (FBS), 4.5 g/L D-glucose, 4 mM L-glutamine, 10 mM non-essential amino acids, 1 mM sodium pyruvate, and 10 mM 4-(2-hydroxyethyl)-1-piperazineethanesulfonic acid (HEPES). Infectious titers of SARS-CoV-2 were determined by the plaque assay in Vero E6 cells in minimum essential media supplemented with 2% FBS, 4 mM L-glutamine, 0.2% BSA, 10 mM HEPES, and 0.12% NaHCO$_3$ and 0.7% agar. 48 h after the addition of plaque overlay, cells were fixed with 5% formaldehyde for 24 h. After the fixation overlay was

removed, cells were stained with 0.2% crystal violet (in 20% EtOH) and plaques were counted.

Quantitative Reverse-Transcription PCR of Viral RNA. qRT-PCR of SARS-Cov-2 RNA was performed as previously described.[103] RNA was extracted from human lung epithelial cells expressing human ACE2 (A549-hACE2) grown in 96-well plates by using the RNeasy 96 Kit (Qiagen) per the manufacturer's instructions. RNA was reverse-transcribed and PCR amplified using Luna Universal One-Step RT-PCR Kit (NEB). SARS-CoV-2 replication was assessed by using primers specific to the N mRNA (forward 5′-CTCTTGTAGATCTGTTCTCTAAACGAAC-3′; reverse 5′-GGTCCACCAAACGTAATGCG-3′). SARS-CoV-2 N mRNA levels were normalized to beta tubulin (forward 5′-GCCTGGACCA-CAAGTTTGAC-3; reverse 5′-TGAAATTCTGGGAGCATGAC-3′). Reactions were run and analyzed on a LightCycler 480 II Instrument (Roche). Relative quantification was calculated by comparing the cycle threshold (C_t) values using $\Delta\Delta C_t$. Significance was determined using a two-tailed unpaired Student's t-test.

Immunofluorescence of Nucleocapsid (N) Protein. Quantification of viral infection was performed as previously described.[103] Briefly, at indicated times after infection A549-hACE2 cells were fixed with 5% formaldehyde and immunostained for nucleocapsid (N) protein. N protein was visualized with a secondary antibody labeled with AlexaFluor-488 (ThermoFisher). SARS-CoV-2 nucleocapsid (N) antibody (clone 1C7C7) was obtained from the Center for Therapeutic Antibody Discovery at the Icahn School of Medicine at Mount Sinai. Nuclei were stained with DAPI. Full wells were imaged and quantified for SARS-CoV-2 infected cells using a Celigo imaging cytometer (Nexcelom Bioscience). All infections with SARS-CoV-2 were performed with three biological replicates.

Five-Day Intranasal Safety Study. Mouse studies were conducted in accordance with the approved University of Colorado IACUC protocol #2807. Female BALB/c mice of age 8−12 weeks, purchased from Envigo (Indianapolis, IN), were divided into groups of five. Each group received either 1, 2, 5, or 10 mg/kg of SBCoV207 intranasally. A control group was administered with sterile PBS. Intranasal administration was achieved by anesthetizing the mouse with isoflurane, holding the mouse at a 45° angle, and gently pipetting 25 μL of SBCoV207 solution into the nostrils.[56] Mice were then monitored for 5 days before being euthanized by cervical dislocation. Cervical dislocation was chosen to preserve the integrity of the lung tissue, which may be damaged by carbon dioxide inhalation euthanasia. Each day of the study, the mouse weight was measured. Prior to euthanasia, blood samples were collected via a submandibular blood draw, and urine samples were collected by palpating the bladder. Once the mouse was euthanized, samples were collected of the brain, lymph node, lung, liver, spleen, and kidney tissue. Collected tissues were rinsed in PBS and either drop-fixed in 10% formalin for histology or immediately frozen at −80 °C for ICP−MS.

Blood samples were allowed to sit on ice for 1 h to clot before being centrifuged at 10,000g for 10 min to collect the serum. The serum was frozen at −80 °C until use in ELISAs. ELISAs for TNF-α and IL-6 (Duoset ELISA, R&D Systems, Minneapolis, MN) and albumin (Immunology Consultants Laboratory, Inc., Portland, OR) were used according to manufacturer directions, with serum diluted 1:100 for TNF-α and IL-6 and 1:500,000 for albumin, and plates were measured at 450 nm in a SpectraMax iD3 plate reader (Molecular Devices, LLC, San Jose, CA) using SoftMax Pro software. Standard curves were built using 4-parameter logistic regression.[104]

Fixed samples were removed to 70% ethanol after 24 h. Histology was performed by Inotiv (Boulder, CO). Formalin-fixed liver, spleen, kidney, and lung samples from mice that received either 10 mg/kg of SBCoV207 or PBS control were processed. Tissues were blocked in paraffin. One slide per block was sectioned at 4 μm and stained with H&E. Glass slides were evaluated by an ACVP-board-certified veterinary pathologist using light microscopy. Histologic findings in each tissue were diagnosed and graded for severity on a 0−5 scale; specifically in this study, alveolar hemorrhage was graded 0 = absent, 1 = minimal (<10% of lung affected), 2 = mild (10−25% of lung affected), 3 = moderate (26−50% of lung affected), 4 = marked (51−

75% of lung affected), and 5 = severe (>75% of lung affected). This scale was also used to assess inflammation in the kidney (mononuclear and neutrophilic, focal, capsule, and with fibrosis) and liver (subacute, multifocal, and random). No histological findings were observed in any spleen samples.

Samples for ICP−MS were later thawed and homogenized in a TissueLyser II bead mill (Qiagen, Germantown, MD) at 30 Hz for 3 min with the addition of 1 μL of deionized water per 1 mg organ tissue. Volumes of homogenates ranging from 10 to 130 μL were then digested in 500 μL of aqua regia (3:1 hydrochloric acid to nitric acid) for 4 h at 100 °C. Pellets were resuspended in 1.5% nitric acid and analyzed with a NexION 2000B single quadropole ICP−MS (PerkinElmer, Waltham, MA). A Meinhard nebulizer was used with a cyclonic glass spray chamber for the introduction of the sample. A nickel sample and skimmer cone were used with an aluminum hyperskimmer cone. The ICP−MS was optimized daily with a calibration solution of 1 ppb In, Ce, Be, U, and Pb. Data were collected using the sample acquisition module in Syngistix software (version 2.3). [197]Au was the analyte monitored. A seven-point linear standard curve was generated at a concentration range of 0−250 ppb. Indium was spiked into each sample at a concentration of 5 ppb. Linearity of the standard curve was defined at an R^2 value of greater than 0.995. The 1000 ppm gold standard solution was purchased from Ricca Chemical Company (Arlington, TX). TraceMetal grade 70% HNO_3 was purchased from ThermoFisher Scientific (Waltham, MA). All H_2O used was from a Milli-Q system (Millipore, Burlington, MA). Data were analyzed using Microsoft Excel by converting measured gold concentrations into ppb (ng/g tissue) via the organ homogenate volume used. This ppb value was then converted into moles of gold, then moles of SBCoV207, per gram of tissue, and finally to ng of SBCoV207 per g of tissue using the molecular weight of the Nanoligomer molecule (27,555.2 g/mol). This was done to provide a clear representation of data consistent with antisense therapeutic data reported in other studies.[88,90,91,94,98] The final conversion factor was 6.358.

Twenty-Four Hour Intranasal Biodistribution Study. Female BALB/c mice of age 8−12 weeks (Envigo, Indianapolis, IN) were divided into groups of five. Each mouse received SBCoV207 intranasally. Blood and urine samples were collected prior to euthanasia at 1, 3, 6, or 24 h after SBCoV207 administration. A small aliquot of 30 μL of whole blood was set aside in a heparin-coated tube for ICP−MS analysis; the remaining blood was kept in a standard tube to clot for serum retrieval. A control group of four mice that received no treatment was also euthanized. Organ samples were collected and analyzed as described above; however, no samples were drop-fixed.

Intraperitoneal Safety and Biodistribution Studies. IP studies followed the same experimental design as IN studies; however, initial drug administration was performed by injecting 100 μL in the peritoneal region of the mouse on the right side of the lower abdomen. Only a single dose of 10 mg/kg was tested. Euthanasia was performed using CO_2 exposure, followed by blood collection via intracardial draw. Urine samples were collected by euthanizing each mouse separately in a clean and empty cage and collecting urine released from the bladder upon death. All other samples were collected similarly to the IN biodistribution study, with the added collection of colon tissue in both the safety and biodistribution studies.

Serum from IP-treated mice was additionally assessed in a 36-plex cytokine/chemokine panel. Quantification of cytokines was performed using 25 μL of serum in Invitrogen Cytokine & Chemokine Convenience 36-Plex Mouse ProcartaPlex Panel 1A (EPXR360-26092-901) following manufacturer's instructions and was analyzed on a Luminex MAGPIX xMAP instrument. The kit measured levels of the following cytokines and chemokines: ENA-78 (CXCL5), Eotaxin (CCL11), GRO-α (CXCL1), IP-10 (CXCL10), MCP-1 (CCL2), MIP-1α (CCL3), MIP-1β (CCL4), MIP-2α (CXCL2), RANTES (CCL5), G-CSF (CSF-3), GM-CSF, IFN-α, IFN-γ, IL-1α, IL-1β, IL-2, IL-3, IL-4, IL-5, IL-6, IL-9, IL-10, IL-12p70, IL-13, IL-15/IL-15R, IL-17A (CTLA-8), IL-18, IL-22, IL-23, IL-27, IL-28, IL-31, LIF,

MCP-3 (CCL7), M-CSF, and TNF-α. Known concentrations of each cytokine/chemokine were used to build standard curves, from which amounts could be calculated per sample.

Intravenous Safety and Biodistribution Studies. IV studies followed the same experimental design as IN and IP studies; however, initial drug administration was performed by injecting 100 μL in the tail vein of the mouse. Each group received either 1, 2, 5, or 10 mg/kg of SBCoV207. All samples were collected and analyzed similarly to the IP biodistribution study.

PK and Percent Biodistribution Analysis. The PK was examined through analyzing data from the 24 h biodistribution study by converting moles of Nanoligomer amounts in different organ tissues into concentrations (mole/volume) by using tissue densities.[64] Briefly, densities of blood (1050 ± 17 kg/m^3), brain (1046 ± 6 kg/m^3), colon (1045 kg/m^3), kidney (1066 ± 56 kg/m^3), liver (1079 ± 53 kg/m^3), lung (1050 kg/m^3), lymph (1019 kg/m^3), and spleen (1089 ± 64 kg/m^3) were used to calculate SBCoV207 concentrations in different organ tissues. Kinetic biodistribution as a percent was estimated in different organs by using their measured Nanoligomer amounts in different organ tissues, and respective estimates of organ masses for 8 week old female BALB/c mice to calculate the fraction (% of total Nanoligomer injected in each animal) of Nanoligomer in different murine organs. Briefly, estimates of different organs: blood (1.5−2.5 mL), urine (0.5−1 mL, large variance in urine volumes leads to higher standard deviation in biodistribution amounts in urine), colon (0.507 ± 0.07 g), kidney (0.274 ± 0.032 g), liver (1.013 ± 0.116 g), lung (0.13 ± 0.013 g), and spleen (0.106 ± 0.008 g) were used to calculate biodistribution in different murine organs.[105,106] Using PK data for IP and IV administration in the blood, and drawing a curve using average values, we estimated AUC and bioavailability (F) for IP administration (F = AUC IP/AUC IV).[65]

Statistical Analysis of Data and Data Visualization. Unless otherwise stated, data were analyzed using Microsoft Excel. p-values for samples were calculated using a student's two-tailed t-test, with significance defined as $p < 0.05$. Data points in box plots were determined to be outliers if measurements were outside the upper or lower quartiles using an interquartile range of 1.5. Standard curves for ELISAs were generated using a four-parameter logistic regression MATLAB (MathWorks) code by Cardillo.[104] Data from the SPR measurements were analyzed using Scrubber 2.0 (BioLogic). Figures 1A,B, 2A, S2A, and S3A were created with BioRender (BioRender.com). Figures 1D and S1D were created with Jupyter (Project Jupyter). Tables S1−S3 were created with Microsoft Office. Figures 3D−G and S5−S7 were images taken by Inotiv (Boulder, CO). All other figures were created with Origin (OriginLab).

■ ASSOCIATED CONTENT

Ⓢ Supporting Information

The Supporting Information is available free of charge at https://pubs.acs.org/doi/10.1021/acsbiomaterials.2c00510.

Sequences for oligomers used; ELISA results; SPR analysis; effects of SBCoV207 intraperitoneal and intravenous administration on mouse body weight; histology analysis; 36-cytokine/chemokine panel tests; SBCoV207 Nanoligomer biodistribution; and intraperitoneal and intravenous percent biodistribution data for blood, kidney, urine, liver, lymph, spleen, and colon (PDF)

■ AUTHOR INFORMATION

Corresponding Author

Anushree Chatterjee − *Department of Chemical and Biological Engineering, University of Colorado Boulder, Boulder, Colorado 80303, United States; Sachi Bioworks, Inc., Louisville, Colorado 80027, United States; Antimicrobial Regeneration Consortium, Boulder, Colorado* 80301, *United States;* ⓞ orcid.org/0000-0002-8389-9917; Email: anushree.chatterjee@gmail.com

Authors

Colleen R. McCollum − *Department of Chemical and Biological Engineering, University of Colorado Boulder, Boulder, Colorado 80303, United States*

Colleen M. Courtney − *Department of Chemical and Biological Engineering, University of Colorado Boulder, Boulder, Colorado 80303, United States; Sachi Bioworks, Inc., Louisville, Colorado 80027, United States*

Nolan J. O'Connor − *Department of Chemical and Biological Engineering, University of Colorado Boulder, Boulder, Colorado 80303, United States*

Thomas R. Aunins − *Department of Chemical and Biological Engineering, University of Colorado Boulder, Boulder, Colorado 80303, United States*

Yuchen Ding − *Department of Chemical and Biological Engineering, University of Colorado Boulder, Boulder, Colorado 80303, United States;* ⓞ orcid.org/0000-0003-1953-5075

Tristan X. Jordan − *Department of Microbiology, New York University Langone, New York, New York 10016, United States*

Keegan L. Rogers − *Department of Pharmaceutical Sciences, University of Colorado Anschutz Medical Campus, Aurora, Colorado 80045, United States*

Stephen Brindley − *Department of Pharmaceutical Sciences, University of Colorado Anschutz Medical Campus, Aurora, Colorado 80045, United States*

Jared M. Brown − *Department of Pharmaceutical Sciences, University of Colorado Anschutz Medical Campus, Aurora, Colorado 80045, United States*

Prashant Nagpal − *Sachi Bioworks, Inc., Louisville, Colorado 80027, United States; Antimicrobial Regeneration Consortium, Boulder, Colorado 80301, United States*

Complete contact information is available at:
https://pubs.acs.org/10.1021/acsbiomaterials.2c00510

Author Contributions

The manuscript was written through contributions of all authors. C.R.M., C.M.C., and A.C. designed the experiments. C.R.M. and C.M.C. conducted 5 day safety studies and biodistribution studies. C.R.M. performed ELISAs and homogenized and digested samples for ICP−MS. P.N. and C.M.C. conducted multi-plex ELISAs on blood serum. N.J.O., T.R.A., and Y.D. synthesized PNAs. P.N. synthesized Nanoligomers. N.J.O. performed SPR analysis. T.X.J. performed A549 cell in vitro studies and qPCR. K.L.R. and S.B. performed ICP−MS. C.R.M., C.M.C., N.J.O., P.N., and A.C. analyzed the experimental data. C.R.M., C.M.C., N.J.O., T.X.J., K.L.R., P.N., and A.C. wrote the manuscript. All authors discussed the results and edited the manuscript. All authors have given approval to the final version of the manuscript.

Notes

The authors declare the following competing financial interest(s): A.C., P.N., and C.M.C. are part of the start-up company Sachi Bioworks that developed this technology.

■ ACKNOWLEDGMENTS

■ REFERENCES

(1) Hu, B.; Guo, H.; Zhou, P.; Shi, Z.-L. Characteristics of SARS-CoV-2 and COVID-19. *Nat. Rev. Microbiol.* **2021**, *19*, 141−154.

(2) Mollica, V.; Rizzo, A.; Massari, F. The Pivotal Role of TMPRSS2 in Coronavirus Disease 2019 and Prostate Cancer. *Future Oncol.* **2020**, *16*, 2029−2033.

(3) Wu, C.; Chen, X.; Cai, Y.; Xia, J. a.; Zhou, X.; Xu, S.; Huang, H.; Zhang, L.; Zhou, X.; Du, C.; Zhang, Y.; Song, J.; Wang, S.; Chao, Y.; Yang, Z.; Xu, J.; Zhou, X.; Chen, D.; Xiong, W.; Xu, L.; Zhou, F.; Jiang, J.; Bai, C.; Zheng, J.; Song, Y. Risk Factors Associated with Acute Respiratory Distress Syndrome and Death in Patients with Coronavirus Disease 2019 Pneumonia in Wuhan, China. *JAMA Intern. Med.* **2020**, *180*, 934−943.

(4) Mortaz, E.; Tabarsi, P.; Varahram, M.; Folkerts, G.; Adcock, I. M. The Immune Response and Immunopathology of COVID-19. *Front. Immunol.* **2020**, *11*, 2037.

(5) Zhang, J.; Xie, B.; Hashimoto, K. Current Status of Potential Therapeutic Candidates for the COVID-19 Crisis. *Brain, Behav., Immun.* **2020**, *87*, 59−73.

(6) Dong, E.; Du, H.; Gardner, L. An interactive web-based dashboard to track COVID-19 in real time. *Lancet Infect. Dis.* **2020**, *20*, 533−534.

(7) Sadoff, J.; Gray, G.; Vandebosch, A.; Cárdenas, V.; Shukarev, G.; Grinsztejn, B.; Goepfert, P. A.; Truyers, C.; Fennema, H.; Spiessens, B.; Offergeld, K.; Scheper, G.; Taylor, K. L.; Robb, M. L.; Treanor, J.; Barouch, D. H.; Stoddard, J.; Ryser, M. F.; Marovich, M. A.; Neuzil, K. M.; Corey, L.; Cauwenberghs, N.; Tanner, T.; Hardt, K.; Ruiz-Guiñazú, J.; Le Gars, M.; Schuitemaker, H.; Van Hoof, J.; Struyf, F.; Douoguih, M. Safety and Efficacy of Single-Dose Ad26.COV2.S Vaccine against Covid-19. *N. Engl. J. Med.* **2021**, *384*, 2187−2201.

(8) Polack, F. P.; Thomas, S. J.; Kitchin, N.; Absalon, J.; Gurtman, A.; Lockhart, S.; Perez, J. L.; Pérez Marc, G.; Moreira, E. D.; Zerbini, C.; Bailey, R.; Swanson, K. A.; Roychoudhury, S.; Koury, K.; Li, P.; Kalina, W. V.; Cooper, D.; Frenck, R. W.; Hammitt, L. L.; Türeci, Ö.; Nell, H.; Schaefer, A.; Ünal, S.; Tresnan, D. B.; Mather, S.; Dormitzer, P. R.; Şahin, U.; Jansen, K. U.; Gruber, W. C. Safety and Efficacy of the BNT162b2 MRNA Covid-19 Vaccine. *N. Engl. J. Med.* **2020**, *383*, 2603−2615.

(9) Baden, L. R.; El Sahly, H. M.; Essink, B.; Kotloff, K.; Frey, S.; Novak, R.; Diemert, D.; Spector, S. A.; Rouphael, N.; Creech, C. B.; McGettigan, J.; Khetan, S.; Segall, N.; Solis, J.; Brosz, A.; Fierro, C.; Schwartz, H.; Neuzil, K.; Corey, L.; Gilbert, P.; Janes, H.; Follmann, D.; Marovich, M.; Mascola, J.; Polakowski, L.; Ledgerwood, J.; Graham, B. S.; Bennett, H.; Pajon, R.; Knightly, C.; Leav, B.; Deng, W.; Zhou, H.; Han, S.; Ivarsson, M.; Miller, J.; Zaks, T. Efficacy and Safety of the MRNA-1273 SARS-CoV-2 Vaccine. *N. Engl. J. Med.* **2021**, *384*, 403−416.

(10) Zhang, W.; Zhao, Y.; Zhang, F.; Wang, Q.; Li, T.; Liu, Z.; Wang, J.; Qin, Y.; Zhang, X.; Yan, X.; Zeng, X.; Zhang, S. The Use of Anti-Inflammatory Drugs in the Treatment of People with Severe Coronavirus Disease 2019 (COVID-19): The Experience of Clinical Immunologists from China. *Clin. Immunol.* **2020**, *214*, 108393.

(11) Naqvi, A. A. T.; Fatima, K.; Mohammad, T.; Fatima, U.; Singh, I. K.; Singh, A.; Atif, S. M.; Hariprasad, G.; Hasan, G. M.; Hassan, M. I. Insights into SARS-CoV-2 Genome, Structure, Evolution, Pathogenesis and Therapies: Structural Genomics Approach. *BBA, Mol. Basis Dis.* **2020**, *1866*, 165878.

(12) Weerahandi, H.; Hochman, K. A.; Simon, E.; Blaum, C.; Chodosh, J.; Duan, E.; Garry, K.; Kahan, T.; Karmen-Tuohy, S. L.; Karpel, H. C.; Mendoza, F.; Prete, A. M.; Quintana, L.; Rutishauser, J.; Santos Martinez, L.; Shah, K.; Sharma, S.; Simon, E.; Stirniman, A. Z.; Horwitz, L. I. Post-Discharge Health Status and Symptoms in Patients with Severe COVID-19. *J. Gen. Intern. Med.* **2021**, *36*, 738−745.

(13) Karkare, S.; Bhatnagar, D. Promising Nucleic Acid Analogs and Mimics: Characteristic Features and Applications of PNA, LNA, and Morpholino. *Appl. Microbiol. Biotechnol.* **2006**, *71*, 575−586.

(14) Kulkarni, J. A.; Witzigmann, D.; Thomson, S. B.; Chen, S.; Leavitt, B. R.; Cullis, P. R.; van der Meel, R. The Current Landscape of Nucleic Acid Therapeutics. *Nat. Nanotechnol.* **2021**, *16*, 630−643.

(15) Pellestor, F.; Paulasova, P. The Peptide Nucleic Acids (PNAs), Powerful Tools for Molecular Genetics and Cytogenetics. *Eur. J. Hum. Genet.* **2004**, *12*, 694−700.

(16) Montazersaheb, S.; Hejazi, M. S.; Charoudeh, H. N. Potential of Peptide Nucleic Acids in Future Therapeutic Applications. *Adv. Pharm. Bull.* **2018**, *8*, 551−563.

(17) Demidov, V. V.; Potaman, V. N.; Frank-Kamenetskil, M. D.; Egholm, M.; Buchard, O.; Sönnichsen, S. H.; Nlelsen, P. E. Stability of Peptide Nucleic Acids in Human Serum and Cellular Extracts. *Biochem. Pharmacol.* **1994**, *48*, 1310−1313.

(18) Zhang, D. Y.; Seelig, G. Dynamic DNA Nanotechnology Using Strand-Displacement Reactions. *Nat. Chem.* **2011**, *3*, 103−113.

(19) Zhang, B.; Tian, T.; Xiao, D.; Gao, S.; Cai, X.; Lin, Y. Facilitating In Situ Tumor Imaging with a Tetrahedral DNA Framework-Enhanced Hybridization Chain Reaction Probe. *Adv. Funct. Mater.* **2022**, *32*, 2109728.

(20) Gerling, T.; Wagenbauer, K. F.; Neuner, A. M.; Dietz, H. Dynamic DNA devices and assemblies formed by shape-complementary, non-base pairing 3D components. *Science* **2015**, *347*, 1446−1452.

(21) Brown, P. N.; Yin, H. PNA-Based MicroRNA Inhibitors Elicit Anti-Inflammatory Effects in Microglia Cells. *Chem. Commun.* **2013**, *49*, 4415−4417.

(22) Gambari, R.; Gasparello, J.; Finotti, A. Peptide Nucleic Acid-Based Targeting of MicroRNAs: Possible Therapeutic Applications for Glioblastoma. *J. Cancer Metastasis Treat.* **2019**, *5*, 55.

(23) Cadoni, E.; Manicardi, A.; Madder, A. PNA-Based MicroRNA Detection Methodologies. *Molecules* **2020**, *25*, 1296.

(24) Barluenga, S.; Winssinger, N. PNA as a Biosupramolecular Tag for Programmable Assemblies and Reactions. *Acc. Chem. Res.* **2015**, *48*, 1319−1331.

(25) Upadhyay, A.; Ponzio, N. M.; Pandey, V. N. Immunological Response to Peptide Nucleic Acid and Its Peptide Conjugate Targeted to Transactivation Response (TAR) Region of HIV-1 RNA Genome. *Oligonucleotides* **2008**, *18*, 329−335.

(26) Tan, A.; Hong, L.; Du, J. D.; Boyd, B. J. Self-Assembled Nanostructured Lipid Systems: Is There a Link between Structure and Cytotoxicity? *Adv. Sci.* **2019**, *6*, 1801223.

(27) Bost, J. P.; Barriga, H.; Holme, M. N.; Gallud, A.; Maugeri, M.; Gupta, D.; Lehto, T.; Valadi, H.; Esbjörner, E. K.; Stevens, M. M.; El-Andaloussi, S. Delivery of Oligonucleotide Therapeutics: Chemical Modifications, Lipid Nanoparticles, and Extracellular Vesicles. *ACS Nano* **2021**, *15*, 13993−14021.

(28) Meng, Z.; Lu, M. RNA Interference-Induced Innate Immunity, off-Target Effect, or Immune Adjuvant? *Front. Immunol.* **2017**, *8*, 331.

(29) Sioud, M. Induction of Inflammatory Cytokines and Interferon Responses by Double-Stranded and Single-Stranded SiRNAs Is Sequence-Dependent and Requires Endosomal Localization. *J. Mol. Biol.* **2005**, *348*, 1079−1090.

(30) Li, N.; Sun, J.; Benet, Z. L.; Wang, Z.; Al-Khodor, S.; John, S. P.; Lin, B.; Sung, M. H.; Fraser, I. D. C. Development of a Cell System for SiRNA Screening of Pathogen Responses in Human and Mouse Macrophages. *Sci. Rep.* **2015**, *5*, 9559.

(31) Santel, A.; Aleku, M.; Keil, O.; Endruschat, J.; Esche, V.; Durieux, B.; Löffler, K.; Fechtner, M.; Röhl, T.; Fisch, G.; Dames, S.; Arnold, W.; Giese, K.; Klippel, A.; Kaufmann, J. RNA Interference in

the Mouse Vascular Endothelium by Systemic Administration of SiRNA-Lipoplexes for Cancer Therapy. *Gene Ther.* **2006**, *13*, 1360−1370.

(32) Trobaugh, D. W.; Klimstra, W. B. MicroRNA Regulation of RNA Virus Replication and Pathogenesis. *Trends Mol. Med.* **2017**, *23*, 80−93.

(33) Mishra, R.; Kumar, A.; Ingle, H.; Kumar, H. The Interplay Between Viral-Derived MiRNAs and Host Immunity During Infection. *Front. Immunol.* **2020**, *10*, 3079.

(34) Nersisyan, S.; Engibaryan, N.; Gorbonos, A.; Kirdey, K.; Makhonin, A.; Tonevitsky, A. Potential Role of Cellular MiRNAs in Coronavirus-Host Interplay. *PeerJ* **2020**, *8*, No. e9994.

(35) Fani, M.; Zandi, M.; Ebrahimi, S.; Soltani, S.; Abbasi, S. The Role of MiRNAs in COVID-19 Disease. *Future Virol.* **2021**, *16*, 301−306.

(36) Mirzaei, R.; Mahdavi, F.; Badrzadeh, F.; Hosseini-Fard, S. R.; Heidary, M.; Jeda, A. S.; Mohammadi, T.; Roshani, M.; Yousefimashouf, R.; Keyvani, H.; Darvishmotevalli, M.; Sani, M. Z.; Karampoor, S. The Emerging Role of MicroRNAs in the Severe Acute Respiratory Syndrome Coronavirus 2 (SARS-CoV-2) Infection. *Int. Immunopharmacol.* **2021**, *90*, 107204.

(37) Schult, P.; Roth, H.; Adams, R. L.; Mas, C.; Imbert, L.; Orlik, C.; Ruggieri, A.; Pyle, A. M.; Lohmann, V. MicroRNA-122 Amplifies Hepatitis C Virus Translation by Shaping the Structure of the Internal Ribosomal Entry Site. *Nat. Commun.* **2018**, *9*, 2613.

(38) Farr, R. J.; Rootes, C. L.; Rowntree, L. C.; Nguyen, T. H. O.; Hensen, L.; Kedzierski, L.; Cheng, A. C.; Kedzierska, K.; Au, G. G.; Marsh, G. A.; Vasan, S. S.; Foo, C. H.; Cowled, C.; Stewart, C. R. Altered MicroRNA Expression in COVID-19 Patients Enables Identification of SARS-CoV-2 Infection. *PLoS Pathog.* **2021**, *17*, No. e1009759.

(39) Zhang, S.; Amahong, K.; Sun, X.; Lian, X.; Liu, J.; Sun, H.; Lou, Y.; Zhu, F.; Qiu, Y. The MiRNA: A Small but Powerful RNA for COVID-19. *Briefings Bioinf.* **2021**, *22*, 1137−1149.

(40) Arghiani, N.; Nissan, T.; Matin, M. M. Role of MicroRNAs in COVID-19 with Implications for Therapeutics. *Biomed. Pharmacother.* **2021**, *144*, 112247.

(41) McDonald, J. T.; Enguita, F. J.; Taylor, D.; Griffin, R. J.; Priebe, W.; Emmett, M. R.; Sajadi, M. M.; Harris, A. D.; Clement, J.; Dybas, J. M.; Aykin-Burns, N.; Guarnieri, J. W.; Singh, L. N.; Grabham, P.; Baylin, S. B.; Yousey, A.; Pearson, A. N.; Corry, P. M.; Saravia-Butler, A.; Aunins, T. R.; Sharma, S.; Nagpal, P.; Meydan, C.; Foox, J.; Mozsary, C.; Cerqueira, B.; Zaksas, V.; Singh, U.; Wurtele, E. S.; Costes, S. V.; Davanzo, G. G.; Galwano, D.; Paccanaro, A.; Meinig, S. L.; Hagan, R. S.; Bowman, N. M.; Wolfgang, M. C.; Altinok, S.; Sapoval, N.; Treangen, T. J.; Moraes-Vieira, P. M.; Vanderburg, C.; Wallace, D. C.; Schisler, J. C.; Mason, C. E.; Chatterjee, A.; Meller, R.; Beheshti, A. Role of MiR-2392 in Driving SARS-CoV-2 Infection. *Cell Rep.* **2021**, *37*, 109839.

(42) Fan, S.; Tian, T.; Chen, W.; Lv, X.; Lei, X.; Zhang, H.; Sun, S.; Cai, L.; Pan, G.; He, L.; Ou, Z.; Lin, X.; Wang, X.; Perez, M. F.; Tu, Z.; Ferrone, S.; Tannous, B. A.; Li, J. Mitochondrial MiRNA Determines Chemoresistance by Reprogramming Metabolism and Regulating Mitochondrial Transcription. *Cancer Res.* **2019**, *79*, 1069−1084.

(43) Shukla, R.; Bansal, V.; Chaudhary, M.; Basu, A.; Bhonde, R. R.; Sastry, M. Biocompatibility of Gold Nanoparticles and Their Endocytotic Fate inside the Cellular Compartment: A Microscopic Overview. *Langmuir* **2005**, *21*, 10644−10654.

(44) Zuber, G.; Weiss, E.; Chiper, M. Biocompatible Gold Nanoclusters: Synthetic Strategies and Biomedical Prospects. *Nanotechnology* **2019**, *30*, 352001.

(45) Kadhim, R. J.; Karsh, E. H.; Taqi, Z. J.; Jabir, M. S. Biocompatibility of Gold Nanoparticles: In-Vitro and In-Vivo Study. *Mater. Today: Proc.* **2021**, *42*, 3041−3045.

(46) Habault, J.; Poyet, J.-L. Recent Advances in Cell Penetrating Peptide-Based Anticancer Therapies. *Molecules* **2019**, *24*, 927.

(47) De Jong, W. H.; Hagens, W. I.; Krystek, P.; Burger, M. C.; Sips, A. J. A. M.; Geertsma, R. E. Particle Size-Dependent Organ

Distribution of Gold Nanoparticles after Intravenous Administration. *Biomaterials* **2008**, *29*, 1912−1919.

(48) Sonavane, G.; Tomoda, K.; Makino, K. Biodistribution of Colloidal Gold Nanoparticles after Intravenous Administration: Effect of Particle Size. *Colloids Surf., B* **2008**, *66*, 274−280.

(49) Duy, J.; Connell, L. B.; Eck, W.; Collins, S. D.; Smith, R. L. Preparation of Surfactant-Stabilized Gold Nanoparticle-Peptide Nucleic Acid Conjugates. *J. Nanopart. Res.* **2010**, *12*, 2363−2369.

(50) Chakrabarti, R.; Klibanov, A. M. Nanocrystals Modified with Peptide Nucleic Acids (PNAs) for Selective Self-Assembly and DNA Detection. *J. Am. Chem. Soc.* **2003**, *125*, 12531−12540.

(51) Anstaett, P.; Zheng, Y.; Thai, T.; Funston, A. M.; Bach, U.; Gasser, G. Synthesis of Stable Peptide Nucleic Acid-Modified Gold Nanoparticles and Their Assembly onto Gold Surfaces. *Angew. Chem., Int. Ed.* **2013**, *52*, 4217−4220.

(52) Cadoni, E.; Rosa-Gastaldo, D.; Manicardi, A.; Mancin, F.; Madder, A. Exploiting Double Exchange Diels-Alder Cycloadditions for Immobilization of Peptide Nucleic Acids on Gold Nanoparticles. *Front. Chem.* **2020**, *8*, 4.

(53) Ghadiri, M.; Young, P.; Traini, D. Strategies to Enhance Drug Absorption via Nasal and Pulmonary Routes. *Pharmaceutics* **2019**, *11*, 113.

(54) Pires, A.; Fortuna, A.; Alves, G.; Falcão, A. Intranasal Drug Delivery: How, Why and What For? *J. Pharm. Pharm. Sci.* **2009**, *12*, 288−311.

(55) Labiris, N. R.; Dolovich, M. B. Pulmonary Drug Delivery. Part I: Physiological Factors Affecting Therapeutic Effectiveness of Aerosolized Medications. *Br. J. Clin. Pharmacol.* **2003**, *56*, 588−599.

(56) Rosseels, V.; Nazé, F.; De Craeye, S.; Francart, A.; Kalai, M.; Van Gucht, S. A Non-Invasive Intranasal Inoculation Technique Using Isoflurane Anesthesia to Infect the Brain of Mice with Rabies Virus. *J. Virol. Methods* **2011**, *173*, 127−136.

(57) Al Shoyaib, A.; Archie, S. R.; Karamyan, V. T. Intraperitoneal Route of Drug Administration: Should It Be Used in Experimental Animal Studies? *Pharm. Res.* **2020**, *37*, 12.

(58) Grossoehme, N. E.; Li, L.; Keane, S. C.; Liu, P.; Dann, C. E.; Leibowitz, J. L.; Giedroc, D. P. Coronavirus N Protein N-Terminal Domain (NTD) Specifically Binds the Transcriptional Regulatory Sequence (TRS) and Melts TRS-CTRS RNA Duplexes. *J. Mol. Biol.* **2009**, *394*, 544−557.

(59) Good, L.; Awasthi, S. K.; Dryselius, R.; Larsson, O.; Nielsen, P. E. Bactericidal antisense effects of peptide-PNA conjugates. *Nat. Biotechnol.* **2001**, *19*, 360−364.

(60) Jensen, K. K.; Ørum, H.; Nielsen, P. E.; Nordén, B. Kinetics for Hybridization of Peptide Nucleic Acids (PNA) with DNA and RNA Studied with the BIAcore Technique. *Biochemistry* **1997**, *36*, 5072−5077.

(61) Taylor, I. Mouse. *Background Lesions in Laboratory Animals*; Saunders Elsevier, 2012, pp 45−72.

(62) Zaias, J.; Mineau, M.; Cray, C.; Yoon, D.; Altman, N. H. Reference Values for Serum Proteins of Common Laboratory Rodent Strains. *J. Am. Assoc. Lab. Anim. Sci.* **2009**, *48*, 387−390.

(63) Natsume, M.; Tsuji, H.; Harada, A.; Akiyama, M.; Yano, T.; Ishikura, H.; Nakanishi, I.; Matsushima, K.; Kaneko, S.-i.; Mukaida, N. Attenuated Liver Fibrosis and Depressed Serum Albumin Levels in Carbon Tetrachloride-Treated IL-6-Deficient Mice. *J. Leukocyte Biol.* **1999**, *66*, 601−608.

(64) Hasgall, P.; Di Gennaro, F.; Baumgartner, C.; Neufeld, E.; Lloyd, B.; Gosselin, M.; Payne, D.; Klingenböck, A.; Kuster, N. IT'IS Database for thermal and electromagnetic parameters of biological tissues. https://itis.swiss/virtual-population/tissue-properties. 2018.

(65) Price, G.; Patel, D. A. *Drug Bioavailability*; StatPearls Publishing: Treasure Island, FL, 2021.

(66) Kasuga, Y.; Zhu, B.; Jang, K.-J.; Yoo, J.-S. Innate Immune Sensing of Coronavirus and Viral Evasion Strategies. *Exp. Mol. Med.* **2021**, *53*, 723−736.

(67) Cameron, M. J.; Bermejo-Martin, J. F.; Danesh, A.; Muller, M. P.; Kelvin, D. J. Human Immunopathogenesis of Severe Acute Respiratory Syndrome (SARS). *Virus Res.* **2008**, *133*, 13−19.

(68) Eller, K. A.; Aunins, T. R.; Courtney, C. M.; Campos, J. K.; Otoupal, P. B.; Erickson, K. E.; Madinger, N. E.; Chatterjee, A. Facile Accelerated Specific Therapeutic (FAST) Platform to Counter Multidrug-Resistant Bacteria. November 21, 2019, bioRxiv:850313.

(69) Eller, K. A.; Aunins, T. R.; Courtney, C. M.; Campos, J. K.; Otoupal, P. B.; Erickson, K. E.; Madinger, N. E.; Chatterjee, A. Facile Accelerated Specific Therapeutic (FAST) Platform Develops Antisense Therapies to Counter Multidrug-Resistant Bacteria. *Commun. Biol.* **2021**, *4*, 331.

(70) Hope, M. J.; Mui, B.; Ansell, S.; Ahkong, Q. F. Cationic lipids, phosphatidylethanolamine and the intracellular delivery of polymeric, nucleic acid-based drugs (Review). *Mol. Membr. Biol.* **1998**, *15*, 1−14.

(71) Zelphati, O.; Szoka, F. C. Cationic Liposomes as an Oligonucleotide Carrier: Mechanism of Action. *J. Liposome Res.* **1997**, *7*, 31−49.

(72) Semple, S. C.; Klimuk, S. K.; Harasym, T. O.; Dos Santos, N.; Ansell, S. M.; Wong, K. F.; Maurer, N.; Stark, H.; Cullis, P. R.; Hope, M. J.; Scherrer, P. Efficient Encapsulation of Antisense Oligonucleotides in Lipid Vesicles Using Ionizable Aminolipids: Formation of Novel Small Multilamellar Vesicle Structures. *Biochim. Biophys. Acta, Biomembr.* **2001**, *1510*, 152−166.

(73) Heyes, J.; Palmer, L.; Chan, K.; Giesbrecht, C.; Jeffs, L.; MacLachlan, I. Lipid Encapsulation Enables the Effective Systemic Delivery of Polyplex Plasmid DNA. *Mol. Ther.* **2007**, *15*, 713−720.

(74) Brader, M. L.; Williams, S. J.; Banks, J. M.; Hui, W. H.; Zhou, Z. H.; Jin, L. Encapsulation State of Messenger RNA inside Lipid Nanoparticles. *Biophys. J.* **2021**, *120*, 2766−2770.

(75) Fenske, D. B.; Chonn, A.; Cullis, P. R. Liposomal Nanomedicines: An Emerging Field. *Toxicol. Pathol.* **2008**, *36*, 21−29.

(76) Yang, L.; Ma, F.; Liu, F.; Chen, J.; Zhao, X.; Xu, Q. Efficient Delivery of Antisense Oligonucleotides Using Bioreducible Lipid Nanoparticles In Vitro and In Vivo. *Mol. Ther.–Nucleic Acids* **2020**, *19*, 1357−1367.

(77) Tang, M.; Zhang, J.; Yang, C.; Zheng, Y.; Jiang, H. Gold Nanoclusters for Bacterial Detection and Infection Therapy. *Front. Chem.* **2020**, *8*, 181.

(78) Bechara, C.; Chai, H.; Lin, P. H.; Yao, Q.; Chen, C. Growth Related Oncogene-Alpha (GRO-a): Roles in Atherosclerosis, Angiogenesis and Other Inflammatory Conditions. *Med. Sci. Monit.* **2007**, *13*, RA87−RA90.

(79) Nakanishi, K. Unique Action of Interleukin-18 on T Cells and Other Immune Cells. *Front. Immunol.* **2018**, *9*, 763.

(80) Ogura, T.; Ueda, H.; Hosohara, K.; Tsuji, R.; Nagata, Y.; Kashiwamura, S.-i.; Okamura, H. Interleukin-18 Stimulates Hematopoietic Cytokine and Growth Factor Formation and Augments Circulating Granulocytes in Mice. *Blood* **2001**, *98*, 2101−2107.

(81) Bossù, P.; Neumann, D.; Del Giudice, E.; Ciaramella, A.; Gloaguen, I.; Fantuzzi, G.; Dinarello, C. A.; Di Carlo, E.; Musiani, P.; Meroni, P. L.; Caselli, G.; Ruggiero, P.; Boraschi, D. IL-18 CDNA Vaccination Protects Mice from Spontaneous Lupus-like Autoimmune Disease. *Proc. Natl. Acad. Sci. U.S.A.* **2003**, *100*, 14181−14186.

(82) Kaur, N.; Aditya, R. N.; Singh, A.; Kuo, T.-R. Biomedical Applications for Gold Nanoclusters: Recent Developments and Future Perspectives. *Nanoscale Res. Lett.* **2018**, *13*, 302.

(83) Rao, G. V. S.; Tinkle, S.; Weissman, D.; Antonini, J.; Kashon, M.; Salmen, R.; Battelli, L.; Willard, P.; Hubbs, A.; Hoover, M. Efficacy of a Technique for Exposing the Mouse Lung to Particles Aspirated from the Pharynx. *J. Toxicol. Environ. Health, Part A* **2003**, *66*, 1441−1452.

(84) Alvites, R. D.; Caseiro, A. R.; Pedrosa, S. S.; Branquinho, M. E.; Varejão, A. S. P.; Maurício, A. C. The Nasal Cavity of the Rat and Mouse-Source of Mesenchymal Stem Cells for Treatment of Peripheral Nerve Injury. *Anat. Rec.* **2018**, *301*, 1678−1689.

(85) Yu, K.; Deng, M.; Naluai-Cecchini, T.; Glass, I. A.; Cox, T. C. Differences in Oral Structure and Tissue Interactions during Mouse vs. Human Palatogenesis: Implications for the Translation of Findings from Mice. *Front. Physiol.* **2017**, *8*, 154.

(86) Park, J.; Park, J.; Pei, Y.; Xu, J.; Yeo, Y. Pharmacokinetics and Biodistribution of Recently-Developed SiRNA Nanomedicines. *Adv. Drug Delivery Rev.* **2016**, *104*, 93−109.

(87) Chen, Y.; Gu, H.; Zhang, D. S.-Z.; Li, F.; Liu, T.; Xia, W. Highly Effective Inhibition of Lung Cancer Growth and Metastasis by Systemic Delivery of SiRNA via Multimodal Mesoporous Silica-Based Nanocarrier. *Biomaterials* **2014**, *35*, 10058−10069.

(88) Geary, R. S.; Norris, D.; Yu, R.; Bennett, C. F. Pharmacokinetics, Biodistribution and Cell Uptake of Antisense Oligonucleotides. *Adv. Drug Delivery Rev.* **2015**, *87*, 46−51.

(89) Amantana, A.; Iversen, P. Pharmacokinetics and Biodistribution of Phosphorodiamidate Morpholino Antisense Oligomers. *Curr. Opin. Pharmacol.* **2005**, *5*, 550−555.

(90) Thompson, J. D.; Kornbrust, D. J.; Foy, J. W.-D.; Solano, E. C. R.; Schneider, D. J.; Feinstein, E.; Molitoris, B. A.; Erlich, S. Toxicological and Pharmacokinetic Properties of Chemically Modified SiRNAs Targeting P53 RNA Following Intravenous Administration. *Nucleic Acid Ther.* **2012**, *22*, 255−264.

(91) Yu, R. Z.; Lemonidis, K. M.; Graham, M. J.; Matson, J. E.; Crooke, R. M.; Tribble, D. L.; Wedel, M. K.; Levin, A. A.; Geary, R. S. Cross-Species Comparison of in Vivo PK/PD Relationships for Second-Generation Antisense Oligonucleotides Targeting Apolipoprotein B-100. *Biochem. Pharmacol.* **2009**, *77*, 910−919.

(92) Geary, R. S.; Yu, R. Z.; Siwkowski, A.; Levin, A. A. Pharmacokinetic/Pharmacodynamic Properties of Phosphorothioate 2′-O-(2-Methoxyethyl)-Modified Antisense Oligonucleotides in Animal and Man. In *Antisense Drug Technology: Principles, Strategies, and Applications*; Crooke, S. T., Ed.; CRC Press: Boca Raton, 2007; pp 305−326.

(93) Zhang, H.; Cook, J.; Nickel, J.; Yu, R.; Stecker, K.; Myers, K.; Dean, N. M. Reduction of Liver Fas Expression by an Antisense Oligonucleotide Protects Mice from Fulminant Hepatitis. *Nat. Biotechnol.* **2000**, *18*, 862−867.

(94) Altmann, K.-H.; Dean, N. M.; Fabbro, D.; Freier, S. M.; Geiger, T.; Haner, R.; Husken, D.; Martin, P.; Monia, B. P.; Muller, M.; Natt, F.; Nicklin, P.; Phillips, J.; Pieles, U.; Sasmor, H.; Moser, H. E. Second Generation of Antisense Oligonucleotides: From Nuclease Resistance to Biological Efficacy in Animals. *Chimia* **1996**, *50*, 168−176.

(95) Hung, G.; Xiao, X.; Peralta, R.; Bhattacharjee, G.; Murray, S.; Norris, D.; Guo, S.; Monia, B. P. Characterization of Target MRNA Reduction through in Situ RNA Hybridization in Multiple Organ Systems Following Systemic Antisense Treatment in Animals. *Nucleic Acid Ther.* **2013**, *23*, 369−378.

(96) Christensen, J.; Litherland, K.; Faller, T.; van de Kerkhof, E.; Natt, F.; Hunziker, J.; Krauser, J.; Swart, P. Metabolism Studies of Unformulated Internally [3H]-Labeled Short Interfering RNAs in Mice. *Drug Metab. Dispos.* **2013**, *41*, 1211−1219.

(97) Christensen, J.; Litherland, K.; Faller, T.; van de Kerkhof, E.; Natt, F.; Hunziker, J.; Boos, J.; Beuvink, I.; Bowman, K.; Baryza, J.; Beverly, M.; Vargeese, C.; Heudi, O.; Stoeckli, M.; Krauser, J.; Swart, P. Biodistribution and Metabolism Studies of Lipid Nanoparticle-Formulated Internally [3H]-Labeled siRNA in Mice. *Drug Metab. Dispos.* **2014**, *42*, 431−440.

(98) Gao, S.; Dagnaes-Hansen, F.; Nielsen, E. J. B.; Wengel, J.; Besenbacher, F.; Howard, K. A.; Kjems, J. The Effect of Chemical Modification and Nanoparticle Formulation on Stability and Biodistribution of SiRNA in Mice. *Mol. Ther.* **2009**, *17*, 1225−1233.

(99) Larson, S. D.; Jackson, L. N.; Chen, L. A.; Rychahou, P. G.; Evers, B. M. Effectiveness of SiRNA Uptake in Target Tissues by Various Delivery Methods. *Surgery* **2007**, *142*, 262−269.

(100) Smith, R. A.; Miller, T. M.; Yamanaka, K.; Monia, B. P.; Condon, T. P.; Hung, G.; Lobsiger, C. S.; Ward, C. M.; McAlonis-Downes, M.; Wei, H.; Wancewicz, E. V.; Bennett, C. F.; Cleveland, D. W. Antisense Oligonucleotide Therapy for Neurodegenerative Disease. *J. Clin. Invest.* **2006**, *116*, 2290−2296.

(101) Li, J.; Yao, Y.; Xu, J.; Zhao, D.; Liu, M.; Shi, S.; Lin, Y. Modulation of the Crosstalk Between Schwann Cells and Macrophages for Nerve Regeneration: A Therapeutic Strategy Based on

Multifunctional Tetrahedral Framework Nucleic Acids System. *Adv. Mater.* **2022**, 2202513.

(102) Eldrup, A. B.; Nielsen, P. E. Peptide Nucleic Acids. *Advances in Amino Acid Mimetics and Peptidomimetics*; Elsevier, 1999, Vol.2.

(103) Daniloski, Z.; Jordan, T. X.; Wessels, H.-H.; Hoagland, D. A.; Kasela, S.; Legut, M.; Maniatis, S.; Mimitou, E. P.; Lu, L.; Geller, E.; Danziger, O.; Rosenberg, B. R.; Phatnani, H.; Smibert, P.; Lappalainen, T.; TenOever, B. R.; Sanjana, N. E. Identification of Required Host Factors for SARS-CoV-2 Infection in Human Cells. *Cell* **2021**, *184*, 92−105.e16.

(104) Cardillo, G. *Four Parameters Logistic Regression—There and Back Again*; Mathworks File Exchange, 2012.

(105) Jiao, Y.; Zhang, J.; Yan, J.; Stuart, J.; Gibson, G.; Lu, L.; Williams, R.; Wang, Y. J.; Gu, W. Differential Gene Expression between Wild-Type and Gulo-Deficient Mice Supplied with Vitamin C. *Genet. Mol. Biol.* **2011**, *34*, 386−395.

(106) The Jackson Laboratory. *Mouse Phenome Database: BALB/CByJ*, 2018.